AD-A236 644

NRL Report 9327

DTIC

Clutter-Doppler Spectral Analysis for a Space-Based Radar

ERIC L. MOKOLE

Target Characteristics Branch
Radar Division

May 10, 1991

Accession For
NTIS GRA&I ☑
DTIC TAB ☐
Unannounced ☐
Justification
By
Distribution/
Availability Codes
Dist | Avail and/or special
A-1

91-01948

QUALITY INSPECTED 3

Approved for public release; distribution unlimited.

91 6 12 027

REPORT DOCUMENTATION PAGE

Form Approved
OMB No 0704-0188

Public reporting burden for this collection of information is estimated to average 1 hour per response, including the time for reviewing instructions, searching existing data sources, gathering and maintaining the data needed, and completing and reviewing the collection of information. Send comments regarding this burden estimate or any other aspect of this collection of information, including suggestions for reducing this burden to Washington Headquarters Services, Directorate for Information Operations and Reports, 1215 Jefferson Davis Highway, Suite 1204, Arlington, VA 22202-4302, and to the Office of Management and Budget, Paperwork Reduction Project (0704-0188), Washington, DC 20503

1. AGENCY USE ONLY *(Leave blank)*

2. REPORT DATE
May 10, 1991

3. REPORT TYPE AND DATES COVERED
Final

4. TITLE AND SUBTITLE
Clutter-Doppler Spectral Analysis
for a Space-Based Radar

5. FUNDING NUMBERS
PE - 62111N
PR - RA11W51, 2559

6. AUTHOR(S)
Eric L. Mokole

7. PERFORMING ORGANIZATION NAME(S) AND ADDRESS(ES)
Naval Research Laboratory
Washington, DC 20375-5000

8. PERFORMING ORGANIZATION REPORT NUMBER
NRL Report 9327

9. SPONSORING/MONITORING AGENCY NAME(S) AND ADDRESS(ES)
Office of Naval Technology
Arlington, Virginia 22217

10. SPONSORING/MONITORING AGENCY REPORT NUMBER

11. SUPPLEMENTARY NOTES

12a. DISTRIBUTION/AVAILABILITY STATEMENT
Approved for public release; distribution unlimited.

12b. DISTRIBUTION CODE

13. ABSTRACT *(Maximum 200 words)*

The impact of worst-case, ionospheric scintillation on the clutter-Doppler spectrum is analyzed for a space-based radar that operates between 100 and 1300 MHz. Analytical expressions for the spectrum are derived for a narrow, Gaussian antenna beam. For nominal system parameters, the analytical expresions, combined with data from the Defense Nuclear Agency's Wideband satellite experiment, are used to compare the relative significance of the components of the clutter-Doppler spread for a range cell and to obtain the clutter-Doppler spread over the antenna's mainlobe. In addition, lower bounds are determined on the achievable reduction in the clutter-Doppler spread of a system.

14. SUBJECT TERMS
Space-based radar
Clutter-Doppler spectrum
Low frequency
Ionospheric scintillation effects
Spectral spreads

15. NUMBER OF PAGES
43

16. PRICE CODE

17. SECURITY CLASSIFICATION OF REPORT
UNCLASSIFIED

18. SECURITY CLASSIFICATION OF THIS PAGE
UNCLASSIFIED

19. SECURITY CLASSIFICATION OF ABSTRACT
UNCLASSIFIED

20. LIMITATION OF ABSTRACT
SAR

NSN 7540-01-280-5500

Standard Form 298 (Rev 2-89)
Prescribed by ANSI Std Z39-18
298-102

CONTENTS

1.0 INTRODUCTION 1

2.0 GEOMETRY OF COORDINATE FRAMES 2

3.0 CLUTTER SPECTRUM 4

- 3.1 TACCAR Correction 4
- 3.2 Analytical Representation of Clutter Spectrum 6
- 3.3 A Special Case 11

4.0 CLUTTER SPECTRUM FROM WIDEBAND DATA 12

- 4.1 Clutter-Doppler Spread Caused by Platform Motion 13
- 4.2 Computation of σ_{SC} 16
- 4.3 Computation of a Mainbeam's Clutter-Doppler Spectrum 19

5.0 SUMMARY 27

6.0 ACKNOWLEDGMENTS 28

7.0 REFERENCES 28

APPENDIX A – Approximation of the Doppler Shift 29

APPENDIX B – Approximation of Average Doppler Shift over Narrow Mainbeams 33

APPENDIX C – Residual Doppler 35

APPENDIX D – Integrals Involving the Antenna Power Gain 36

CLUTTER-DOPPLER, SPECTRAL ANALYSIS FOR A SPACE-BASED RADAR

1.0 INTRODUCTION

The effect of strong ionospheric scintillation on the total, clutter-Doppler spectrum incurred by a monostatic space-based radar (SBR) system, whose orbit is above the ionosphere and whose carrier frequency is between 100 and 1300 MHz, is analyzed. This work is a continuation of the analysis begun in (Mokole and Knepp 1991) and is based on satellite data obtained from the Defense Nuclear Agency's Wideband satellite experiment of the late 1970s (Fremouw et al. 1978).

In addition to the standard moving-target-indicator (MTI) concept of designing Doppler filters to detect targets of unknown velocity, an SBR's design must account for clutter spread caused by ionospheric scintillation, platform motion relative to the Earth's surface, and intrinsic clutter that consists of radar instabilities and internal motion on the Earth's surface. If the mean Doppler shift and the shape of the clutter spectrum are known, Doppler processors can maximize the detection of moving targets (Andrews 1976; Andrews and Gerlach 1989). The performance of optimal filters is heavily dependent on the width of the clutter-Doppler spectrum. Therefore, all nonstochastic contributions to the spectral width must be removed. Consequently, the components of the clutter-Doppler spectrum are analyzed to determine their relative significance. One goal is to make the minimum detectable velocity (MDV) as small as possible by canceling the clutter. To get the precise relationship between the spectral spread and the MDV, one must consider the implementation of the clutter canceller, the required improvement factor, and the required probabilities of detection and false alarm. This is beyond the scope of this report, but a qualitative indication of the MDV may be obtained by comparing the relative sizes of the spectral components. Generally, the MDV increases with clutter spread.

The clutter-Doppler spectrum is the result of three contributions: (1) the intrinsic clutter that is backscattered from the Earth's surface; (2) the clutter spectrum resulting from ionospheric scintillation experienced by the signal along the propagation path; and (3) the spectrum caused by the motion of the satellite relative to the Earth in the antenna beam. The first two are stochastic in nature and are assumed to be statistically independent, while the third contribution is strictly deterministic. The spectral contributions associated with the random processes are represented by Gaussian functions. When the deterministic contribution is also represented by a Gaussian function, this permits the use of a more tractable formula to calculate the total clutter spread for each range cell.

Following the work of (Andrews 1976; Knepp and Dana 1985), a formula for the clutter-Doppler spectrum is derived for an arbitrary antenna pattern. This formula is applied for a Gaussian pattern relative to certain angular coordinates and reduces to a particularly simple form for a range cell, when certain conditions apply. Specifically, the functional dependence is also Gaussian,

$$S_{CL}(f) = \frac{K}{\sqrt{2\pi}\sigma_{CL}} \exp\left(-\frac{(f-f_0)^2}{2\sigma_{CL}^2}\right); \tag{1}$$

where

$$\sigma_{CL}^2 = \sigma_{IN}^2 + \sigma_{SC}^2 + \sigma_{PM}^2, \tag{2}$$

Manuscript approved 27 March 1991

K is a constant, f_0 is a translation in frequency, and σ_{IN}, σ_{SC}, σ_{PM} are the spreads caused by intrinsic backscatter, scintillation induced by the ionosphere, and platform motion, respectively. Values are then obtained for the three clutter spreads for the Wideband satellite pass (ANCON 08904) that experienced the most severe ionospheric scintillation. The designation, ANCON 08904, represents the data set that was received at the Ancon (Peru) site on the eighty-ninth day (089) of 1977 at 4 a.m. (04). The results are then compared to determine the relative effects of each component. The spreads attributable to scintillation and platform motion are calculated from analytical formulae, while a representative value of the intrinsic clutter is specified from previous measurements. Since the expression for σ_{SC} is easily derived, attention is focused on the derivation of a formula for σ_{PM}. In addition, σ_{SC} is computed for all Ancon passes, and its cumulative distribution is obtained.

2.0 GEOMETRY OF COORDINATE FRAMES

For this problem, the position of the satellite in space is referenced relative to three fundamental, orthogonal, coordinate systems (6 Bate, Ch. 2; ADCOM 1977, Section 2). These reference frames differ primarily in choice of origin and fundamental reference plane. The origins are the points on the Earth's surface (a topocentric system), at the center of the Earth (a geocentric system), and in the satellite (a vehicle-centered system).

The geocentric system, usually denoted "Earth-Centered Inertial," is nonrotating. Its fundamental plane is the equator, the X–axis points in the direction of the vernal equinox, the Z–axis points toward the North Pole, and the Y–axis is chosen so that the system is right-handed. The unit vectors along the X–, Y–, Z–axes respectively are $\underline{\mathrm{I}}$, $\underline{\mathrm{J}}$, $\underline{\mathrm{K}}$.

Since the observations of the Wideband satellite were made relative to two ground stations at Ancon and Kwajalein, a topocentric horizon system is necessary. In particular, the location of the radar is the origin. The coordinate axes are denoted X_h, Y_h, and Z_h, with the positive X_h– and Y_h–axes pointing south and east, respectively, in the plane that is tangent to the Earth's surface, while the Z_h–axis points radially outward from the Earth's center (up). The associated unit vectors are $\underline{\mathrm{S}}$, $\underline{\mathrm{E}}$, and $\underline{\mathrm{Z}}$. The radar sites measured the range and direction to the satellite. "The range is simply the magnitude of the vector $[-\underline{\mathrm{R}}_S]$. The direction ... is determined by two angles which can be picked off the gimbal axes on which the radar antenna [was] mounted [(Bate et al. 1971, p.84)]." The azimuth angle Az was measured clockwise from the negative X_h–axis (north), and the elevation angle El was measured from the projection of the radar line-of-sight onto the X_hY_h–plane to the line-of-sight $(-\underline{\mathrm{R}}_S)$.

The satellite-fixed frame has axes pointing in the nadir (positive z) and satellite-velocity (positive x) directions. The remaining axis (y) completes the right-handed system. When discussing the antenna pattern, spherical coordinates of this reference frame are handy. Define the spherical coordinates (r, ϕ, θ) by

$$\begin{aligned} x &= r\cos\theta\sin\phi \\ y &= r\sin\theta\sin\phi \\ z &= r\cos\phi, \end{aligned} \tag{3}$$

where $\theta \in [0, 2\pi]$ and $\phi \in [0, \pi]$.

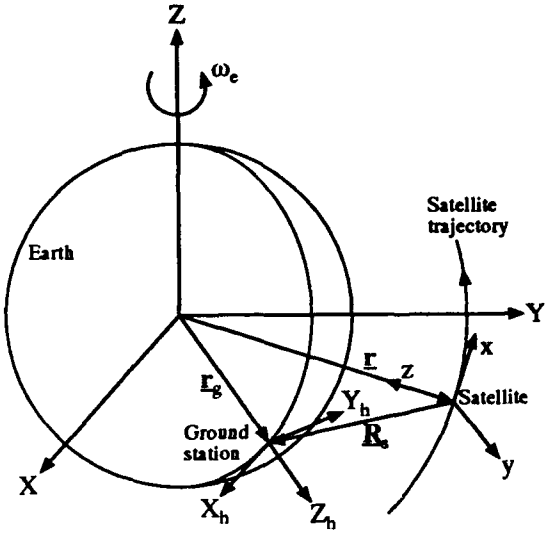

Fig 1(a) – The geocentric, topocentric, and vehicle-centered coordinate frames. $\underline{w} = \omega_e \underline{K}$ is the angular velocity of the rotating Earth. This figure is not drawn to scale.

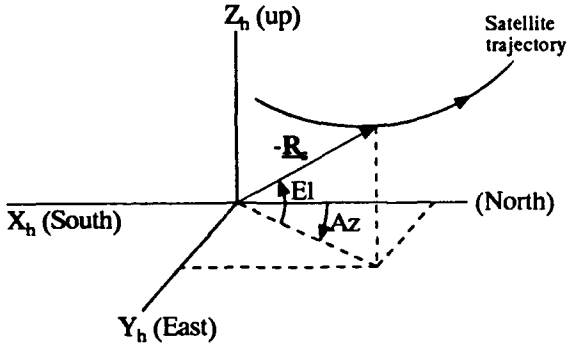

Fig. 1(b) – The topocentric coordinate frame

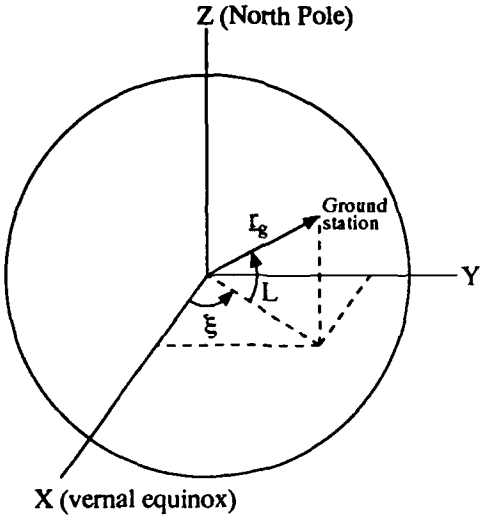

Fig. 1(c) – The Earth-centered, inertial (geocentric), coordinate frame

3.0 CLUTTER SPECTRUM

An MTI system must remove the nonstochastic contributions (platform motion) to the clutter spread. Two systems that compensate for platform motion are generally used: the Time Averaged Clutter Coherent Airborne Radar (TACCAR) and the Displaced Phase Center Antenna (DPCA) systems. TACCAR is a phase-locked system that was designed by MIT Lincoln Laboratory to remove the average Doppler shift of the clutter, whereas the DPCA concept uses antenna and MTI techniques to remove the spectral spreading induced by platform motion (Andrews 1976; Andrews 1978).

Figure 2 illustrates the effect of platform motion and ionospheric scintillation on the clutter spectrum that is observed in their absence. In particular, Fig 2(a) depicts a relatively narrow, zero-mean spectrum caused by intrinsic clutter for a stationary platform, no ionospheric irregularities, and no ionospheric motion. The combined intrinsic-clutter and ionospheric effects are visible in Fig. 2(b), where the scintillation-producing irregularities result in spectral spreading. Ionospheric motion is assumed negligible; thus translation of the spectral peak is insignificant. Figure 2(c) shows the translation $\bar{f}_D$ and additional spreading of the spectrum from platform motion and the antenna pattern.

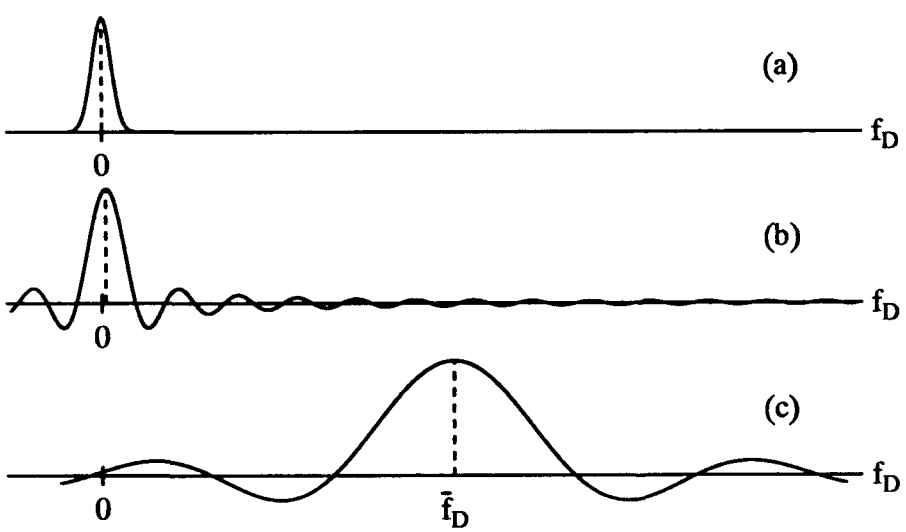

Fig. 2 — (a) Intrinsic clutter spectrum for a fixed platform with no ionosphere, (b) clutter spectrum that includes the effect of the ionosphere for a stationary platform, and (c) clutter spectrum includes ionospheric and platform motion effects

First, the translational effect is removed by applying a clutter-locking technique (Shrader and Gregers-Hansen 1990; Andrews and Gerlach 1989) like TACCAR. This effectively centers the notch of the response of the clutter cancellation processor at the average value $\bar{f}_D$ of the clutter spectrum, which is necessary for good performance of processors like MTI and DPCA.

By assuming a TACCAR-like correction, the resulting clutter spectrum is derived for any clutter patch within the antenna beam. Results are then derived for the antenna's mainlobe, which are then simplified under certain assumptions.

3.1 TACCAR Correction

Let a scatterer on the Earth's surface be located at $P_S = (R_S, \phi_S, \theta_S)$ relative to the satellite-based coordinate frame; let $\underline{R}_S$ be the position vector to the scatterer; let $P_a = (R_a, \phi_a, \theta_a)$ be

the coordinates where the antenna's pointing axis (boresight) intersects the Earth's surface; let h be the satellite's altitude; let α be the grazing angle; and let v_p be the speed of the satellite (Fig 3). For SBRs above the ionosphere, $\phi_a \in [0, \pi/2)$. Since the Earth is rotating, P_S is moving with velocity $\underline{v}_e$. Hence the velocity of the platform relative to P_S is $\underline{v}_r = \underline{v}_p - \underline{v}_e$, and the Doppler shift of the scatterers at P_S in the direction $\underline{R}_S$ is

$$f_D = \frac{2f_t}{c}\left(\underline{v}_r \cdot \hat{\mathbf{R}}_S\right) = \frac{2f_t v_r}{c}\cos\gamma_r \simeq \frac{2f_t v_r}{c}\cos\gamma_S = \frac{2f_t v_r}{c}\sin\phi_S\cos\theta_S \simeq \frac{2f_t v_p}{c}\sin\phi_S\cos\theta_S, \quad (4)$$

where f_t is the transmission frequency, $\hat{\mathbf{R}}_S$ is the unit vector $\underline{R}_S/R_S$, γ_S is the angle from $\underline{v}_p$ to $\underline{R}_S$, γ_r is the angle from $\underline{v}_r$ to $\underline{R}_S$, and c is the speed of propagation (2.99792458×10^8 m/s). For analytical manipulations, it is easier to use γ_S instead of γ_r. This is done in the remainder of the report. However, for greater accuracy, the equations after this point should be rederived with $\cos\gamma_r = \sin\phi_r\cos\theta_r$, where ϕ_r and γ_r are the spherical angles specified by Eq.(3) for the vector $\underline{v}_r$. The goodness of the approximations in Eq.(4) at the altitudes considered here is discussed in Section 4 and Appendix A.

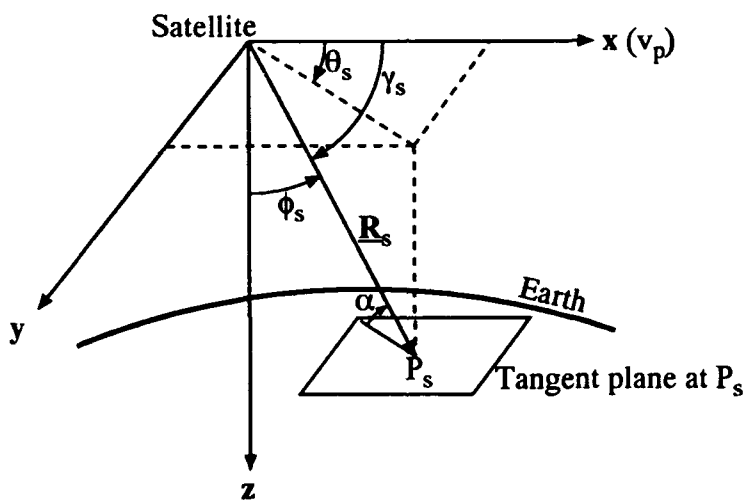

Fig. 3 — The geometry of a scatterer on the Earth's surface relative to the vehicle-centered coordinate frame

If $\mathcal{A}$ is the ground patch illuminated by the antenna's radiation pattern and if Ω is the corresponding set of angles (ϕ, θ), the average Doppler shift over the ground patch is

$$\bar{f}_D = \frac{1}{\text{Area}(\mathcal{A})}\iint_{\mathcal{A}} f_D(r, \phi, \theta)\, d\mathcal{A}. \quad (5)$$

A common practice (Andrews 1976; Knepp and Dana 1985) is to integrate over the projection Ω of the antenna pattern onto a reference sphere of radius R_0 about the origin of the satellite-fixed frame, instead of integrating over the surface area $\mathcal{A}$. This inherently assumes that f_D is

independent of $\underline{R}_S$; however, f_D does depend indirectly on $\underline{R}_S$ through the relative speed v_r. Since the difference between the minimum and maximum ranges to the illuminated ground patch of the mainbeam can be as large as 540 km (292 nm), it is unclear whether this approximation is accurate. To determine the legitimacy of this approximation, one must derive the relationship between the coordinates of the satellite-based and earth-centered-inertial frames, calculate the Jacobian of this transformation, mathematically describe the surface patch, and evaluate the integrals in Eq.(5). Since determining the validity of the approximation is a nontrivial undertaking, this work uses it without justification, but cautions that the results will reflect any errors inherent in its usage.

In addition to the preceding assumptions, suppose that the clutter over small solid angles is isotropic and homogeneous. Therefore (see Appendix B for details),

$$\bar{f}_D \simeq \frac{1}{\text{Area}(\Omega)} \iint_{\Omega} f_D \, d\Omega = \frac{2 f_t v_r}{c} \cos\theta_a \sin\phi_a, \tag{6}$$

where $d\Omega = R_0^2 \sin\phi \, d\phi d\theta$. The TACCAR-like correction f_D' to the Doppler shift is obtained by subtracting the estimated average Doppler from the Doppler shift:

$$f_D' = f_D - \bar{f}_D = \frac{2 f_t v_r}{c} \left[\cos\theta_S \sin\phi_S - \cos\theta_a \sin\phi_a\right],$$

or for $(\phi, \theta) \in \Omega$,

$$f_D'(\phi,\theta) = \frac{2 f_t v_r}{c} \left[\cos\theta \sin\phi - \cos\theta_a \sin\phi_a\right]. \tag{7}$$

3.2 Analytical Representation of Clutter Spectrum

The received, Doppler-corrected, clutter voltage V_{CL} for a monostatic radar is analytically modeled as

$$V_{CL}(t,r,\phi,\theta) = V(r,\phi,\theta) A_{IN}(t,\phi,\theta) A_{SC}(t,\phi,\theta) \exp\left(i 2\pi t f_D'(\phi,\theta)\right), \tag{8}$$

where t is the local clock time of the receiver and (r,ϕ,θ) is given by Eq.(3). The quantity V represents the received voltage for nonfluctuating clutter and is directly proportional to G^2/r^2, the ratio of the two-way antenna gain to the range squared. In particular, the expression $V = C_0 G^2/r^2$ is used in the remainder of the report. The parameter C_0 is the constant 1 V-m^2 so that the dimension of C_0/r^2 is volts. The factors A_{IN} and A_{SC} are the dimensionless envelope fluctuations caused by random variations of the surface clutter and the electron density along the two-way, ionospheric propagation path, respectively. Hence

$$V_{CL}(t,r,\phi,\theta) = C_0 \frac{G^2(\phi,\theta)}{r^2(\phi,\theta)} A_{IN}(t,\phi,\theta) A_{SC}(t,\phi,\theta) \exp\left(i 2\pi t f_D'(\phi,\theta)\right), \tag{9}$$

The random processes A_{IN} and A_{SC} result from entirely different physical mechanisms and, consequently, are statistically independent.

The autocorrelation R_{CL} of V_{CL} is

$$R_{CL}(\tau,\phi,\theta) = \langle V_{CL}(t+\tau,\phi,\theta) V_{CL}^*(\tau,\phi,\theta)\rangle. \tag{10}$$

The angular brackets denote statistical expectation, and the superscripted asterisk denotes complex conjugation. Substituting Eq.(9) into Eq.(10) leads to

$$R_{CL}(r,\tau,\phi,\theta) = \frac{C_0^2}{r^4(\phi,\theta)} |G(\phi,\theta)|^4 \left\langle A_{IN}(t+\tau) A_{IN}^*(t) \exp\left(2\pi i \tau f_D'(\phi,\theta)\right) A_{SC}(t+\tau) A_{SC}^*(t)\right\rangle. \tag{11}$$

Since A_{IN} and A_{SC} are statistically independent, the expectation in Eq.(11) becomes a product of expectations. Hence

$$\begin{aligned} R_{CL}(r,\tau,\phi,\theta) &= \frac{C_0^2}{r^4(\phi,\theta)}|G(\phi,\theta)|^4\langle A_{IN}(t+\tau)A_{IN}^*(t)\exp\big(2\pi i\tau f_D'(\phi,\theta)\big)\rangle\langle A_{SC}(t+\tau)A_{SC}^*(t)\rangle \\ &= \frac{C_0^2}{r^4(\phi,\theta)}|G(\phi,\theta)|^4\exp\big(2\pi i\tau f_D'(\phi,\theta)\big)R_{IN}(\tau)R_{SC}(\tau), \end{aligned} \tag{12}$$

where R_{IN} and R_{SC} are the autocorrelations of the intrinsic and propagation envelopes, respectively.

The Fourier transform of R_{CL} is the clutter spectrum S_{CL} in the direction (ϕ,θ) of the antenna pattern:

$$\begin{aligned} S_{CL}(f,\phi,\theta) &= \mathcal{F}\Big\{\frac{C_0^2}{r^4(\phi,\theta)}|G(\phi,\theta)|^4\exp\big(2\pi i\tau f_D'(\phi,\theta)\big)R_{IN}(\tau)R_{SC}(\tau)\Big\} \\ &= \frac{C_0^2}{r^4(\phi,\theta)}|G(\phi,\theta)|^4\mathcal{F}\Big\{\exp\big(2\pi i\tau f_D'(\phi,\theta)\big)R_{IN}(\tau)\Big\} * \mathcal{F}\Big\{R_{SC}(\tau)\Big\} \\ &= \frac{C_0^2}{r^4(\phi,\theta)}|G(\phi,\theta)|^4 S_{IN}\big(f - f_D'(\phi,\theta)\big) * S_{SC}(f). \end{aligned} \tag{13}$$

The asterisk symbolizes the operation of convolution, and $\mathcal{F}$ is the Fourier transformation operator. Although an asterisk represents two mathematical operations, it should be clear from the context whether an asterisk denotes convolution or complex conjugation. Note that S_{CL} is a convolution of the clutter spectrum caused by scintillation S_{SC} and the translation of f_D' of the spectrum from motion on the Earth's surface S_{IN}.

To treat the total clutter spectrum of a portion of the antenna beam, in particular, the surface subtended by the solid angle corresponding to the mainbeam of the antenna pattern, the transform representing the spectrum for a given direction (Eq.(13)) must be integrated over the appropriate angles. The spectrum is first analyzed for incremental subregions of A. This requires nomenclature that relates an incremental region to the satellite-fixed reference frame.

The mainbeam ground patch (Fig. 4) is naturally subdivided by range cells (radial) corresponding to unambiguous range R_u [$= c/(2f_r)$), where f_r is the pulse repetition frequency]. These unambiguous range cells are further partitioned into N_r subcells, with

$$N_r = \left[\!\!\left[\frac{R_u}{\text{Range Resolution}}\right]\!\!\right] = \left[\!\!\left[\frac{2R_u}{c\tau_c}\right]\!\!\right] = \left[\!\!\left[\frac{1}{2f_r\tau_c}\right]\!\!\right]. \tag{14}$$

The double brackets denote the greatest integer function, and τ_c is the compressed pulsewidth.

Since the range does not change appreciably within each range cell, it is assumed constant therein. For constant range r and arbitrary θ, the relationship between r and ϕ is

$$r = R_e\left[\frac{h+R_e}{R_e}\cos\phi - \sqrt{1-\Big(\frac{h+R_e}{R_e}\sin\phi\Big)^2}\right]. \tag{15}$$

Only angles out to the optical horizon are considered so that ϕ lies in $\big[0, \arcsin\big(R_e/(h+R_e)\big)\big]$. The right endpoint is the angle associated with the optical horizon and corresponds to a zero grazing angle ($\alpha = 0$). Equation (15) is always well-defined for this interval.

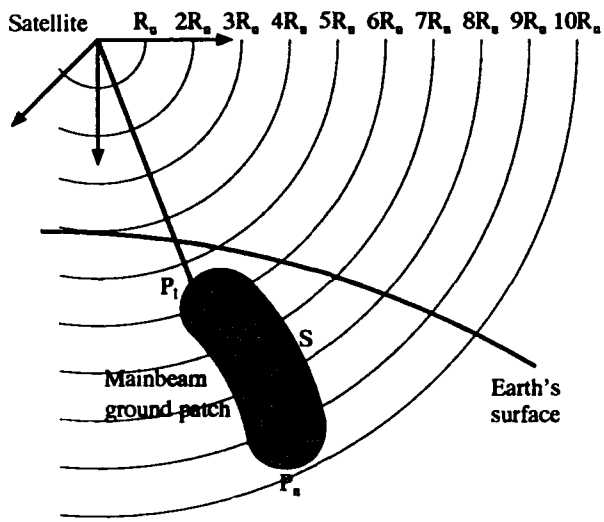

Fig. 4 — The projection of an antenna pattern's mainbeam onto the Earth's surface. The solid curve within the ground patch corresponds to the antenna's boresight.

The number M_0 of unambiguous range intervals covered by the mainbeam's ground patch depends on ϕ_a and the beamwidth ($\Delta\phi$) in the ϕ direction. As ϕ_a and $\Delta\phi$ increase, so do the number of unambiguous intervals. Suppose that M and $M+M_0-1$ are natural numbers associated with the left endpoints of the first and last unambiguous range intervals of the ground patch, respectively, and that $m \in \{1,\ldots,M_0\}$ denotes the mth of these unambiguous intervals (see Fig. 5(a)). Therefore $[(M+m-1)R_u,(M+m)R_u]$ represents the mth interval. As stated earlier, each interval has N_r range cells. The nth range cell of the mth unambiguous interval is specified by

$$\left[\left(M+m-1+\frac{n-1}{N_r}\right)R_u,\left(M+m-1+\frac{n}{N_r}\right)R_u\right].$$

The composition of the mth interval is depicted in Fig. 5(b). Clearly M_0N_r range cells completely cover the mainbeam's ground patch.

Let $[\theta^l_{mn},\theta^u_{mn}]$ demarcate the antenna's mainbeam beamwidth in the $\underline{\theta}$ direction (azimuthal beamwidth). Consider the clutter spectrum S^{mn}_{CL} of the nth range cell of the mth unambiguous range interval associated with the ground patch. To obtain S^{mn}_{CL}, the transform of Eq.(13) must be integrated over the surface

$$A_{mn}=\left\{(r,\phi,\theta): r\in\left[\left(M+m-1+\frac{n-1}{N_r}\right)R_u,\left(M+m-1+\frac{n}{N_r}\right)R_u\right],\right.$$
$$\left.\phi\in[\phi^l_{mn},\phi^l_{mn}],\quad\text{and}\quad\theta\in[\theta^l_{mn},\theta^l_{mn}]\right\}.$$

However, on each range cell, r (and hence ϕ) is assumed constant. Arbitrarily choose the constant value of r to be the midpoint of the r-interval of A_{mn} and denote it by r_{mn}. The corresponding value ϕ_{mn} of ϕ can be obtained from Eq.(15) by solving for ϕ and substituting r_{mn} for r.

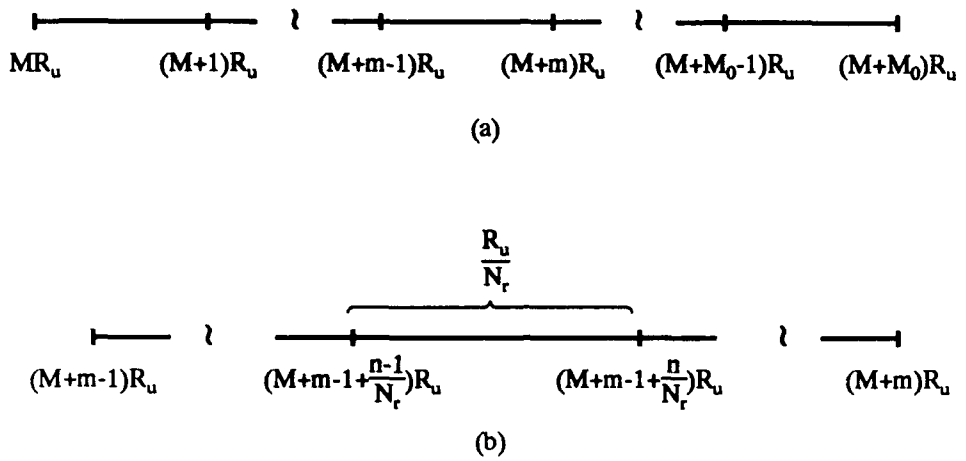

Fig. 5 — (a) The M_0 unambiguous range intervals within the antenna's mainbeam, and (b) the N_r range cells of the mth unambiguous range interval in the mainbeam

Under these assumptions, the integral is evaluated over the set

$$\Omega_{mn} = \left\{(\phi,\theta) : \phi \in \left[\phi^l_{mn}, \phi^l_{mn}\right], \theta \in \left[\theta^l_{mn}, \theta^l_{mn}\right]\right\},$$

where $r(\phi) \simeq r_{mn}$. Thus

$$\begin{aligned} S^{mn}_{CL}(f) &= \iint_{\Omega_{mn}} \frac{C_0^2}{r^4(\phi)} |G(\phi,\theta)|^4 S_{IN}\big(f - f'_D(\phi,\theta)\big) * S_{SC}(f)\, d\Omega \\ &\simeq \frac{C_0^2}{r^4_{mn}} \int_{\phi^l_{mn}}^{\phi^u_{mn}} \int_{\theta^l_{mn}}^{\theta^u_{mn}} |G(\phi_{mn},\theta)|^4 \\ &\qquad \times S_{IN}\big(f - f'_D(\phi_{mn},\theta)\big) * S_{SC}(f) r^2_{mn} \sin\phi_{mn}\, d\phi d\theta \\ &= \frac{C_0^2(\phi^u_{mn} - \phi^l_{mn})\sin\phi_{mn}}{r^2_{mn}} \int_{\theta^l_{mn}}^{\theta^u_{mn}} |G(\phi_{mn},\theta)|^4 \\ &\qquad \times S_{IN}\big(f - f'_D(\phi_{mn},\theta)\big) * S_{SC}(f)\, d\theta. \end{aligned} \tag{16}$$

Equation (16) expresses S^{mn}_{CL} as an integral of a convolution. For a slightly different perspective, take the inverse Fourier transform of Eq.(16), interchange limits of integration, and apply some transform properties to get

$$R^{mn}_{CL}(\tau) = \frac{C_0^2(\phi^u_{mn} - \phi^l_{mn})\sin\phi_{mn}}{r^2_{mn}} R_{IN}(\tau) R_{SC}(\tau) \int_{\theta^l_{mn}}^{\theta^u_{mn}} |G(\phi_{mn},\theta)|^4 \exp\big(2\pi i \tau f'_d(\phi_{mn},\theta)\big)\, d\theta, \tag{17}$$

which is the autocorrelation of the total clutter spectrum incurred by the surface within the (m,n)th range cell. Clearly it consists of three terms: the individual autocorrelations of the intrinsic and propagation envelopes and a function that in some sense adds up the Doppler effect over the antenna beam. Denote the product of the integral and the constants in Eq.(17) by $R^{mn}_{PM}(\tau)$. Thus

$$R^{mn}_{PM}(\tau) = \frac{C_0^2(\phi^u_{mn} - \phi^l_{mn})\sin\phi_{mn}}{r^2_{mn}} \int_{\theta^l_{mn}}^{\theta^u_{mn}} |G(\phi_{mn},\theta)|^4 \exp\big(2\pi i \tau f'_d(\phi_{mn},\theta)\big)\, d\theta, \tag{18}$$

$$R_{CL}^{mn}(\tau) = R_{IN}^{mn}(\tau) R_{SC}^{mn}(\tau) R_{PM}^{mn}(\tau). \tag{19}$$

Upon taking the Fourier transform of the preceding equation and defining S_{PM}^{mn} to be the Fourier transform of R_{PM}^{mn}, one arrives at the general expression

$$S_{CL}^{mn}(f) = \left(S_{IN}^{mn}(f) * S_{SC}^{mn}(f) \right) * S_{PM}^{mn}(f) \tag{20}$$

for the total clutter spectrum of the (m,n)th range cell. This power spectral density is the convolution of the power spectral densities of the backscatter and propagation envelopes and a function that incorporates the deterministic clutter contribution in the antenna's beam from the Doppler associated with the motion of the satellite.

Since an antenna pattern is usually referenced relative to its boresight, introduce two new coordinates $\bar{\phi}$ and $\bar{\theta}$ that represent the position relative to boresight (ϕ_a, θ_a); that is,

$$\bar{\phi} = \phi - \phi_a \qquad \text{and} \qquad \bar{\theta} = \theta - \theta_a. \tag{21}$$

In Eq.(16), make the change of variable specified by Eq.(21) to obtain

$$S_{CL}^{mn}(f) = \frac{C_0^2(\phi_{mn}^u - \phi_{mn}^l)\sin\phi_{mn}}{r_{mn}^2} \int_{\theta_{mn}^l - \theta_a}^{\theta_{mn}^u - \theta_a} |\mathcal{G}(\bar{\phi}_{mn}, \bar{\theta})|^4 S_{IN}^{mn}(f - F_D^l(\bar{\phi}_{mn}, \bar{\theta})) * S_{SC}^{mn}(f)\, d\bar{\theta}, \tag{22}$$

where

$$\begin{aligned} F_D^l(\bar{\phi}_{mn}, \bar{\theta}) &= f_D^l(\bar{\phi}_{mn} + \phi_a, \bar{\theta} + \theta_a), \\ \mathcal{G}(\bar{\phi}_{mn}, \bar{\theta}) &= G(\bar{\phi}_{mn} + \phi_a, \bar{\theta} + \theta_a). \end{aligned} \tag{23}$$

For narrow mainbeams, the translated Doppler correction F_D^l is approximated by (Appendix C)

$$F_{DA}^l(\bar{\phi}_{mn}, \bar{\theta}) = B\bar{\phi}_{mn} + A\bar{\theta}, \tag{24(a)}$$

where

$$\begin{aligned} w_1 &= \frac{2 f_t v_r}{c}, \\ A &= -w_1 \sin\theta_a \sin\phi_a, \\ B &= w_1 \cos\theta_a \cos\phi_a. \end{aligned} \tag{24(b)}$$

For an SBR with a low pulse repetition frequency (PRF), only the clutter-Doppler spectrum of an individual range cell is needed in developing an effective signal processor. On the other hand, a high-PRF SBR simultaneously receives returns from multiple, ambiguous range cells in the mainbeam. Consequently, one must consider the spectrum generated by all of the ambiguous range cells associated with a given range over the entire mainbeam when developing the signal processor. In this report, the high-PRF case is considered. The set of complex clutter returns (voltages), which are obtained by integrating over each range cell, are assumed to be statistically independent and to have zero means. Consequently, the corresponding autocorrelations R_{CL}^{mn} and spectra S_{CL}^{mn} are additive components of the total autocorrelation and total spectrum of the mainbeam; that is,

$$\bar{R}_{CL}(\tau) = \sum_{n=1}^{N_r} \left\{ \sum_{m=1}^{M_0} R_{CL}^{mn}(\tau) \right\} \qquad \text{and} \qquad \bar{S}_{CL}(f) = \sum_{n=1}^{N_r} \left\{ \sum_{m=1}^{M_0} S_{CL}^{mn}(f) \right\}. \tag{25}$$

The parenthetical expressions are the superpositions of the autocorrelations (R_{CL}^n) and spectra (S_{CL}^n), respectively, of the nth range cells of each unambiguous range interval within the mainbeam. Equation (25) is written in this manner because a receiver cannot distinguish among $S_{CL}^{1n}, \ldots, S_{CL}^{M_0 n}$; instead it lumps them together as S_{CL}^n for each n. One typically says that the clutter from each of these range cells folds over into one value, as though the summed clutter spectrum comes from one range cell. The contributions from the sidelobes are ignored.

3.3 A Special Case

Equation (20) has a rather simple form and facilitates further simplifications for some functions. In particular, suppose S_β^{mn} is Gaussian with zero-mean and standard deviation σ_β for $\beta \in \{IN, SC\}$; that is,

$$S_\beta^{mn}(f) = \frac{1}{\sqrt{2\pi}\sigma_\beta} \exp\left(-\frac{f^2}{2\sigma_\beta^2}\right). \tag{26}$$

Therefore, the convolution of S_{IN}^{mn} and S_{SC}^{mn} becomes

$$\frac{1}{\sqrt{2\pi}\sqrt{\sigma_{IN}^2 + \sigma_{SC}^2}} \exp\left(-\frac{f^2}{2(\sigma_{IN}^2 + \sigma_{SC}^2)}\right).$$

Hence

$$S_{CL}^{mn}(f) = \frac{1}{\sqrt{2\pi}\sqrt{\sigma_{IN}^2 + \sigma_{SC}^2}} \exp\left(-\frac{f^2}{2(\sigma_{IN}^2 + \sigma_{SC}^2)}\right) * S_{PM}^{mn}(f). \tag{27}$$

Upon taking the Fourier transform of Eq.(3[illegible]), with the change of variable given by Eq.(21), observe that

$$\begin{aligned} S_{PM}^{mn}(f) &= \int_{-\infty}^{\infty} \int_{\vartheta_{mn}^l}^{\vartheta_{mn}^u} \frac{C_0^2(\phi_{mn}^u - \phi_{mn}^l)\sin\phi_{mn}}{r_{mn}^2} |\mathcal{G}(\bar{\phi}_{mn}, \bar{\theta})|^4 \exp\left(2\pi i \tau F_D'(\bar{\phi}_{mn}, \bar{\theta})\right) \exp(-2\pi i f \tau)\, d\bar{\theta} d\tau \\ &= \frac{C_0^2(\phi_{mn}^u - \phi_{mn}^l)\sin\phi_{mn}}{r_{mn}^2} \int_{\vartheta_{mn}^l}^{\vartheta_{mn}^u} |\mathcal{G}(\bar{\phi}_{mn}, \bar{\theta})|^4 \delta\left(f - F_D'(\bar{\phi}_{mn}, \bar{\theta})\right) d\bar{\theta}, \end{aligned} \tag{28}$$

where δ is the Dirac delta, $\vartheta_{mn}^l = \theta_{mn}^l - \theta_a < 0$, and $\vartheta_{mn}^u = \theta_{mn}^u - \theta_a > 0$. Formally substituting Eq.(28) into Eq.(27), interchanging the order of integration, and applying the sifting property of the Dirac delta yield

$$S_{CL}^{mn}(f) = \frac{C_0^2(\phi_{mn}^u - \phi_{mn}^l)\sin\phi_{mn}}{r_{mn}^2\sqrt{2\pi}\sqrt{\sigma_{IN}^2 + \sigma_{SC}^2}} \int_{\vartheta_{mn}^l}^{\vartheta_{mn}^u} |\mathcal{G}(\bar{\phi}_{mn}, \bar{\theta})|^4 \exp\left(-\frac{\left(f - F_d'(\bar{\phi}_{mn}, \bar{\theta})\right)^2}{2(\sigma_{IN}^2 + \sigma_{SC}^2)}\right) d\bar{\theta}. \tag{29}$$

It is tacitly assumed that the mathematical operations resulting in Eq.(29) are valid over the class of functions that are considered.

An explicit representation of the antenna pattern is required for there to be any chance of getting a closed form expression for S_{CL}^{mn}. Even when the pattern is specified, a closed-form expression is difficult to obtain. Usually one must resort to a numerical evaluation of Eq.(29). However, for a Gaussian-shaped antenna pattern having circles in the $(\bar{\phi}, \bar{\theta})$–coordinate frame, an explicit representation of S_{CL}^{mn} is obtained; specifically, it is now shown that Eq.(29) reduces to Eq.(1), when a certain approximation is valid.

Let the one-way, power gain of the antenna be characterized by

$$\left|G(\bar{\phi}, \bar{\theta})\right|^2 = g_0 \exp\left(-\frac{\bar{\phi}^2 + \bar{\theta}^2}{(\eta/2)^2}\right); \tag{30}$$

where g_0 is the power gain at boresight, and η is a constant that is chosen so that the power gain within the mainlobe is 95% of the total, two-way gain. For narrow mainbeams, F_D' is approximated by $B\bar{\phi}_{mn} + A\bar{\theta}$ (Eq.(24)). In this case, the level curves of the two-way gain $|\mathcal{G}|^4$ are circles in the

$(\bar{\phi}, \bar{\theta})$–coordinate frame. Note that these level curves are not the cross sections of the antenna pattern that are perpendicular to the boresight. Define $2p_0$ to be the desired, mainlobe beamwidth. Since the Gaussian pattern has no nulls, interpret this to mean that 95% of the power is in the region $0 \leq \bar{\phi}^2 + \bar{\theta}^2 \leq p_0^2$, which implies that $\eta = p_0\sqrt{8/\ln(20)}$ (see Appendix D).

With the Gaussian power gain and a narrow mainbeam, Eq.(29) reduces to

$$S_{CL}^{mn}(f) = 2\Big[\mathrm{erf}(t_{mn}^u) - \mathrm{erf}(t_{mn}^l)\Big]\frac{K_{mn}}{\sqrt{2\pi}\sigma_{CL}}\exp\left(-\frac{(f - B\bar{\phi}_{mn})^2}{2\sigma_{CL}^2}\right), \tag{31}$$

where

$$\begin{aligned}
\sigma_{PM} &= \frac{|A|\eta}{4} = \frac{\eta}{4}\frac{2f_t v_r}{c}|\sin\theta_a|\sin\phi_a, \\
\sigma_{CL}^2 &= \sigma_{IN}^2 + \sigma_{SC}^2 + \sigma_{PM}^2, \\
K_{mn} &= g_0^2\frac{\eta\sqrt{\pi}}{2\sqrt{2}}\frac{C_0^2(\phi_{mn}^u - \phi_{mn}^l)\sin\phi_{mn}}{r_{mn}^2}\exp\left(-\frac{8\phi_{mn}^2}{\eta^2}\right), \\
t_{mn}^l &= \frac{4\sigma_{CL}}{\eta\sqrt{2(\sigma_{IN}^2 + \sigma_{SC}^2)}}\left[-\vartheta_{mn}^u - \frac{A\eta^2(f - \bar{\phi}_{mn})}{16\sigma_{CL}^2}\right], \\
t_{mn}^u &= \frac{4\sigma_{CL}}{\eta\sqrt{2(\sigma_{IN}^2 + \sigma_{SC}^2)}}\left[+\vartheta_{mn}^u - \frac{A\eta^2(f - \bar{\phi}_{mn})}{16\sigma_{CL}^2}\right], \\
\mathrm{erf}(z) &= \frac{2}{\sqrt{\pi}}\int_0^z \exp(-x^2)\,dx.
\end{aligned} \tag{32}$$

When the integral in Eq.(29) closely approximates

$$\int_{-\infty}^{\infty} |\mathcal{G}(\bar{\phi}_{mn}, \bar{\theta})|^4 \exp\left(-\frac{(f - F_d'(\bar{\phi}_{mn}, \bar{\theta}))^2}{2(\sigma_{IN}^2 + \sigma_{SC}^2)}\right) d\bar{\theta}, \tag{33}$$

S_{CL}^{mn} is approximately

$$S_{CL,A}^{mn}(f) = \frac{K_{mn}}{\sqrt{2\pi}\sigma_{CL}}\exp\left(-\frac{(f - B\bar{\phi}_{mn})^2}{2\sigma_{CL}^2}\right). \tag{34}$$

Therefore, when this approximation is valid, the clutter-Doppler spectrum within a range cell is characterized by an expression having the form of Eq.(1).

Clearly, the approximation is not good for range cells at the heel and toe of the mainbeam's footprint, that is, for $\bar{\phi}_{mn} \simeq \pm p_0$. For further details, see Appendix D. Since Eq.(34) is simpler than Eq.(31), it is more desirable for analytical purposes; however, it may result in errors, and one should be cognizant of this.

4.0 CLUTTER SPECTRUM FROM WIDEBAND DATA

The 1977 Wideband data (Fremouw et al. 1978; Knepp and Mokole 1991) are used to extrapolate the clutter-Doppler spectrum and spreads for a sea-clutter patch and for the Gaussian power gain of Eq.(31). Although these data correspond to severe, ionospheric-scintillation conditions for 1977, the clutter-Doppler spread caused by scintillation is not the worst (largest), since the data were measured at the end of a period of solar minimum.

Data from 22 satellite passes are used to construct a distribution of σ_{CL}. In particular, σ_{CL} is computed for the satellite pass (ANCON 08904) that experienced the most intense scintillation; that is, the values of τ_0 are the smallest (Mokole and Knepp 1991; Knepp and Mokole 1991). The Ancon receiver site was located at -11.767° latitude and -77.500° longitude. The orbit of ANCON 08904 is chosen as representative of a retrograde, circular, nearly polar orbit at an altitude of approximately 1030 km. The position of this pass, measured from Ancon, allows estimation of v_r, ϕ_a, and θ_a.

The total clutter-Doppler spread depends on three parameters: σ_{IN}, σ_{SC}, σ_{PM}. A typical value for worst-case, clutter-Doppler spread σ_{IN} for internal motion of the sea is 1 m/s (Shrader and Gregers-Hansen 1990, Table 15.1, p.15.9), whereas the scintillation spread σ_{SC} is determined from an analytical formula that depends on τ_0. According to Eq.(34), σ_{PM} is calculable once the antenna's beamwidth $2p_0$ and the parameters v_r, ϕ_a, θ_a are specified. This report considers narrow mainbeams on the order of 1° to 2°; so a nominal value of $p_0 = 1°$ is selected. The individual clutter-Doppler spreads are compared, and their importance relative to σ_{CL} is discussed. In addition, examples are considered to determine whether Eq.(34), the approximation of Eq.(31), may be used to calculate the total, clutter-Doppler spectrum.

4.1 Clutter-Doppler Spread Caused by Platform Motion

Since σ_{PM} depends on ϕ_a, θ_a, v_r, and since these parameters depend on a satellite's orbit, orbital data pertinent to ANCON 08904 is discussed. The satellite was launched by the P76-5 Scout Rocket on 22 May 1976. The orbital elements and associated information (Table 1) are determinable from a North American Aerospace Defense Command (NORAD) pass planner and (King–Hele et al. 1988). The orbital elements of Table 1 are used to create an input orbit for the most current version of the Fast Orbital Prediction Program (FOPP8) (Eisele and Shannon 1975) that most closely matches the NORAD orbital data. With this facsimile orbit, FOPP8 calculates ϕ_a, θ_a, R_a. Then the range outputs (R_a) of FOPP8 are used to estimate v_r, which is used to calculate σ_{PM}.

Table 1 — Orbital Elements of Wideband Satellite

SSDC No.	08860
International No.	1976-47A
Launch Date	22.32 May 1976
Expiration Date	400 yr
Payload	P76-5
Inclination Angle	1.73953751649 rad
Eccentricity	0.054830209
Angle of Right Ascension	6.27122910366 rad
Angle of Perigee from Ascending Node	1.60201995295 rad
Normalized Semi-Major Axis	1.1608806
Mean Motion	0.0594559435781
Greenwich Hour @ Epoch	2.57899235231 min
Period	105.5 min
Perigee Height	996 km
Apogee Height	1060 km

The time of each data point (Table 2) is the local mean solar time at the Greenwich meridian, variously called Greenwich Mean Time (GMT), Universal Time (UT), or Zulu (Z) time (Bate et al.

1971). The entry 4:4:30.0 means 4 hr, 4 min, and 30 sec in the morning at Greenwich. The azimuthal Az and elevation El angles are measured in the topocentric frame at Ancon (Fig. 1(b)), while the latitude (Lat) and longitude (Lon) are measured with respect to the rotating, Earth-centered frame with 0°–longitudinal meridian passing through Greenwich. From the latitudes of Table 2, a north-to-south equatorial crossing occurs between 4:6:30.0 and 4:7:30.0. To make use of the data, assume that the mainbeam of a hypothetical antenna points at Ancon; hence $R_S = R_a$. The ranges R_a generated by FOPP8 are not exactly those of the NORAD pass planners, however they are close enough to permit calculation of v_r. The angles ϕ_a and θ_a correspond to the parameters DipAngle $+\pi/2$ and BackAz, respectively, of FOPP8.

Table 2 — Orbital Data Relative To Ancon

UT (hr:min:s)	Az (Deg)	El (Deg)	Lat(+N) (Deg)	Lon(+E) (Deg)	R_a (km)	ϕ_a (Deg)	θ_a (Deg)
4:04:30.0	23.6	10.4	8.1	-68.6	2822.4480	58.297	346.34
4:05:30.0	25.5	15.8	4.7	-69.4	2453.3444	56.503	344.68
4:06:30.0	28.1	22.4	1.3	-70.2	2097.0196	53.516	342.25
4:07:30.0	32.3	30.9	-2.0	-71.1	1762.7336	48.752	338.48
4:08:30.0	39.8	42.0	-5.4	-71.9	1467.5248	41.427	331.68
4:09:30.0	56.1	55.7	-8.8	-72.7	1240.6548	31.188	317.52
4:10:30.0	96.6	65.8	-12.2	-73.5	1125.6456	21.731	282.61
4:11:00.0	124.1	64.7	-13.8	-74.0	1156.2036	24.411	232.50
4:12:00.0	157.9	52.8	-17.2	-74.8	1322.3280	35.007	207.69
4:13:00.0	171.3	39.7	-20.6	-75.7	1581.2376	44.066	197.24
4:14:00.0	177.8	29.3	-23.9	-76.6	1894.5960	50.231	191.86
4:15:00.0	-178.5	21.4	-27.2	-77.6	2238.6976	54.182	188.64
4:16:00.0	-176.2	15.1	-30.6	-78.6	2600.3932	56.632	186.50

Since R_a is the distance measured in the topocentric frame at Ancon, $\dot{\underline{R}}_a$ is the relative radial velocity $\underline{v}_r$. According to Eq.(A17) of Appendix A,

$$\underline{v}_r \cdot \hat{\mathbf{R}}_S = \underline{v}_r \cdot \hat{\mathbf{R}}_a = -\dot{R}_a,$$

where $\dot{R}_a$ is the amplitude of $\dot{\underline{R}}_a$. However, the approximation

$$\underline{v}_r \cdot \hat{\mathbf{R}}_a = v_r \cos\gamma_r \simeq v_r \cos\gamma_a = v_r \sin\phi_a \cos\theta_a$$

implies that

$$v_r \simeq \left| \frac{\dot{R}_a}{\sin\phi_a \cos\theta_a} \right|, \tag{35}$$

provided the denominator is not zero. Therefore, to estimate the speed v_r at a particular time t_0 of the orbit, the following difference scheme is employed,

$$\left|\dot{R}_a(t_0)\right| = \left|\underline{v}_r \cdot \hat{\mathbf{R}}_a\right| = \left(v_r \sin\phi_a |\cos\theta_a|\right)\Big|_{t=t_0} \simeq \left| \frac{R_a(t_0 + \frac{\Delta t}{2}) - R_a(t_0 - \frac{\Delta t}{2})}{\Delta t} \right|, \tag{36}$$

where a time increment Δt of 2.4 s is chosen. Substituting Δt and R_a from Table 3 into Eq.(36) yields the estimates of v_r. These speeds are listed in Table 4 with the other parameters that are necessary in computing σ_{PM}. By Eqs.(24(b)), (32), and (35),

$$\sigma_{PM} = \frac{\pi}{720}\sqrt{\frac{8}{\ln 20}}\,\frac{2f_t|\dot{R}_a|}{c}\,|\tan\theta_a|, \tag{37}$$

if $\cos\theta_a \neq 0$. The evaluations of Eq.(37) for 137.6748 MHz (VHF), 413.0244 MHz (UHF), and 1239.0730 MHz (L-band) are also provided by Table 4. Clearly, σ_{PM} increases with increasing frequency.

Table 3 — Ranges and Universal Times For Ancon

UT (hr:min:s)	R_a (km)	UT (hr:min:s)	R_a (km)	UT (hr:min:s)	R_a (km)
4:04:28.8	2829.8560	4:09:28.8	1244.3588	4:12:58.8	1575.4964
4:04:30.0	2822.4480	4:09:30.0	1240.6548	4:13:00.0	1581.2376
4:04:31.2	2814.8548	4:09:31.2	1237.1360	4:13:01.2	1587.1640
4:05:28.8	2460.5672	4:10:28.8	1126.5716	4:13:58.8	1887.9288
4:05:30.0	2453.3444	4:10:30.0	1125.6456	4:14:00.0	1894.5960
4:05:31.2	2445.9364	4:10:31.2	1124.7196	4:14:01.2	1901.2632
4:06:28.8	2103.8720	4:10:58.8	1154.1664	4:14:58.8	2231.6600
4:06:30.0	2097.0196	4:11:00.0	1156.2036	4:15:00.0	2238.6976
4:06:31.2	2089.9820	4:11:01.2	1158.2408	4:15:01.2	2245.7352
4:07:28.8	1769.2156	4:11:58.8	1317.8832	4:15:58.8	2592.9852
4:07:30.0	1762.7336	4:12:00.0	1322.3280	4:16:00.0	2600.3932
4:07:31.2	1756.4368	4:12:01.2	1326.7728	4:16:01.2	2607.6160
4:08:28.8	1472.8956				
4:08:30.0	1467.5248				
4:08:31.2	1462.1540				

Table 4 — Clutter-Doppler Spread From Platform Motion at Ancon

ϕ_a (deg)	θ_a (deg)	$\|\dot{R}_a\|$ (km/s)	v_r (km/s)	σ_{PM}@VHF (Hz)	σ_{PM}@UHF (Hz)	σ_{PM}@L-band (Hz)
58.297	346.34	6.2505	7.5606	9.95	29.85	89.54
56.503	344.68	6.0962	7.5797	10.94	32.81	98.43
53.516	342.25	5.7875	7.5580	12.13	36.40	109.19
48.752	338.48	5.3245	7.6124	13.75	41.25	123.75
41.427	331.68	4.4757	7.6840	15.80	47.39	142.16
31.188	317.52	3.0095	7.8799	18.05	54.14	162.43
21.731	282.61	0.7717	9.5471	22.59	67.77	203.30
24.411	232.50	1.6977	6.7479	14.49	43.47	130.40
35.007	207.69	3.7040	7.2917	12.73	38.19	114.57
44.066	197.24	4.8615	7.3189	9.88	29.64	88.92
50.231	191.86	5.5560	7.3861	7.64	22.92	68.77
54.182	188.64	5.8647	7.3155	5.84	17.51	52.52
56.632	186.50	6.0962	7.3467	4.55	13.65	40.94

4.2 Computation of σ_{SC}

When severe scintillation conditions exist, the autocorrelation R_{SC} (Eqs. (11) and (12)) of the envelope fluctuation A_{SC}, which are caused by ionospheric scintillation, is Gaussian (Mokole and Knepp 1991); that is,

$$R_{SC}(\tau) = \left\langle A_{SC}(t+\tau,\phi,\theta)A^*_{SC}(t,\phi,\theta)\right\rangle = e^{-\tau^2/\tau_0^2}.$$

The parameter τ_0 is called the complex decorrelation time. If propagating pulses are separated in time by an amount less than τ_0, they are presumed coherent. It is assumed that R_{SC} is constant with respect to small changes in ϕ and θ. Since the line of sight between the Wideband satellite and Ancon changes slowly over the orbit, this assumption holds. Equation (37) implies that

$$S_{SC}(f) = \frac{1}{\sqrt{2\pi}\sigma_{SC}} \exp\left(\frac{-f^2}{2\sigma_{SC}^2}\right), \qquad \sigma_{SC} = \frac{1}{\pi\tau_0\sqrt{2}}. \tag{38}$$

Clearly, S_{SC} spreads (σ_{SC} increases) as τ_0 decreases. For severe scintillation, $\tau_0 < 0.25$ s. Figure 6 provides histograms of the measured values of τ_0 for all the Ancon satellite passes at VHF, UHF, and L-band. As the frequency increases, the percentage of τ_0 at the smaller values decreases. In particular, slightly more than 23% of the values of τ_0 are below 0.25 s at VHF. In contrast, less than 3.5% and 0.11% of the τ_0 are below 0.25 s at UHF and L-band, respectively. Although not shown in Fig. 6, 17.45%, 44.81%, and 70.76% of the τ_0 are greater than 8.392 s at VHF, UHF, and L-band. Additionally, the minimum value for each frequency is 0.024 s. The measured minima are not exact but are limited by the integration time of the Wideband receiver and the sampling interval (2 ms). Hence 24 ms is probably not the actual minimum τ_0; however, values less than 24 ms occur infrequently, since this value is not measured often.

Figure 7 displays the distribution of σ_{SC}, corresponding to the measured values of τ_0, for each frequency. For 99% of the data, σ_{SC} is less than 4.66 Hz, 1.38 Hz, 0.22 Hz, respectively, at VHF, UHF, L-band. Clearly, this spectral spread decreases to very small values as the frequency increases. To get a worst-case (largest) value of σ_{SC}, substitute the smallest value of τ_0 (0.024 s) into Eq.(38) to obtain 9.38 Hz for the three frequencies. These values are then used in Eqs.(31) and (34).

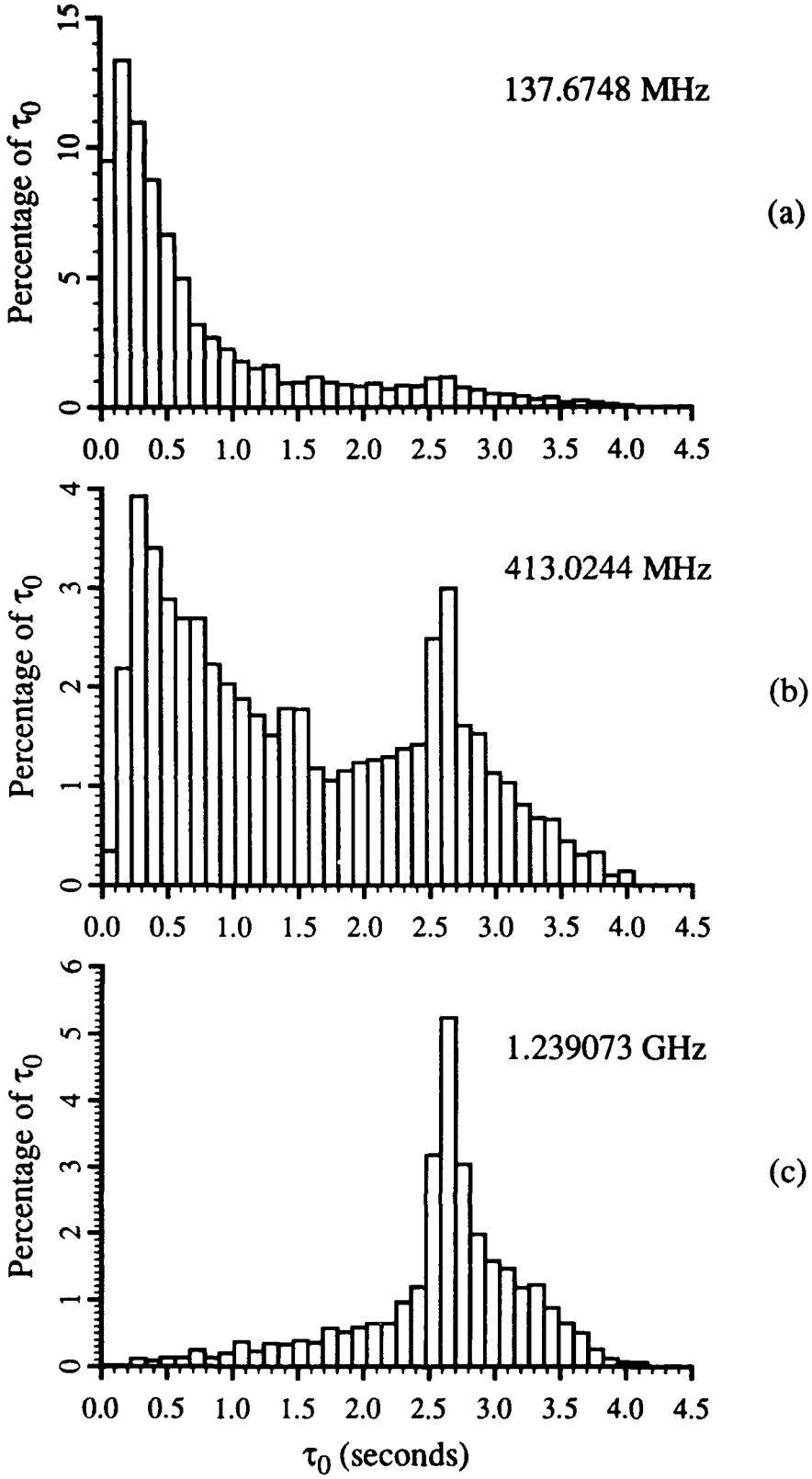

Fig. 6 — Occurence percentage of τ_0 at VHF, UHF, and L-band for 1977 Ancon satellite passes. Although not pictured, 17.45%, 44.81%, and 70.76% of the τ_0 are > 4.5 sec at VHF, UHF, L-band, respectively.

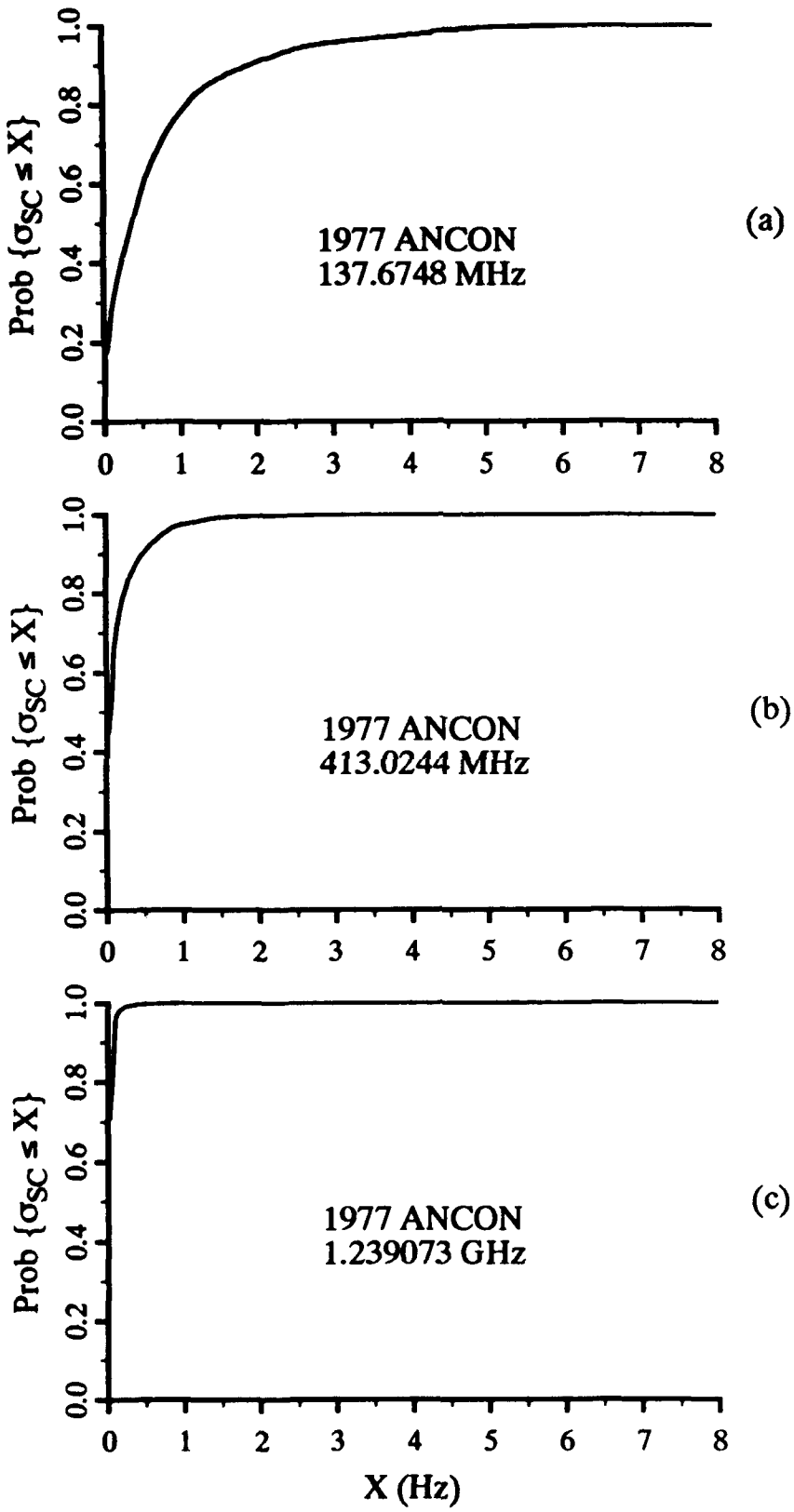

Fig. 7 – Cumulative distribution of the clutter spread σ_{SC} caused by ionospheric scintillation for the 1977 Ancon satellite passes at VHF, UHF, and L-band

4.3 Computation of a Mainbeam's Clutter-Doppler Spectrum

To determine the total, clutter-Doppler spread of a mainbeam, consider the spectra $\bar{S}_{CL}$ and $\bar{S}_{CL,A}$, obtained by substituting Eqs.(31) and (34) into Eq.(25). These spectra are graphed for nominal values of τ_c, h, f_r, p_0 (1 μs, 1030 km, 577 Hz, 1°) and for five sets of (v_r, ϕ_a, θ_a) at the three frequencies. Recall that τ_c, h, f_r, and p_0 are the compressed pulsewidth, satellite's altitude, PRF, and one-half beamwidth. Three of the sets are taken from the Ancon data (the dark boxes in Table 4 and lines 1 to 3 of Table 5). The remaining two sets are $(0, 21.731°, 282.61°)$ and $(7789.230\,\text{m/s}, 58.297°, 90°)$. Approximate values of v_r for the data (Sets 1 to 3) are generated from Eq.(35), with an exception discussed below, while Sets 4 and 5 are chosen so that σ_{PM} is extremized for a 1030-km orbit.

Table 5 — Five Sets of Data

Set #	ϕ_a (Deg)	θ_a (Deg)	v_r (km/s)	M
1	58.297	346.34	7.5606	4
2	21.731	282.61	7.7892	1
3	56.632	186.50	7.3467	2
4	21.731	282.61	0.0000	1
5	58.297	90.00	6.6364	4

Since

$$v_r^2 = \underline{v}_r \cdot \underline{v}_r = v_p^2 + v_e^2 - 2(\underline{v}_p \cdot \underline{v}_e),$$

the maximum value of v_r is attained when $\underline{v}_e$ and $\underline{v}_p$ are antiparallel. Hence

$$v_r \leq v_p + v_e. \tag{39}$$

By Eqs. (37) and (39), an upper bound for σ_{PM} is

$$\frac{\pi}{720}\sqrt{\frac{8}{\ln 20}}\frac{2f_t}{c}(v_p + v_e), \tag{40}$$

where the speeds v_e and v_p are calculated in Appendix A.

Recall from Eq.(15) that only angles ϕ out to the optical horizon 59.425° are considered; that is, $\phi_a < 58.425°$ for a 2° antenna beamwidth ($2p_0$). Consequently, for a 1030-km orbit, $|\sin\phi_a| \leq 0.852$ and

$$v_r \leq 0.852(v_p + v_e) \simeq (0.852)(7.78923\frac{\text{km}}{\text{s}} = 6.6364\frac{\text{km}}{\text{s}}. \tag{41}$$

Therefore, 6.6364 km/s is the maximum achievable value of v_r for this orbit; however, observe that this value is exceeded in Sets 1 to 3 of Table 5. This merely indicates that the approximation (Eq.(37)), used to calculate v_r for the data, is an overestimate. In lieu of no velocity measurement and incomplete orbital data, the inexactitude (upper bound) in the calculation of v_r is accepted. The exception is Set 2, where the value 9.5471 km/s of Table 4 is replaced with $v_p + v_e = 7.7892$ km/s to compensate for the poor approximation of $\underline{v}_r \cdot \hat{\mathbf{R}}_S$ by $\underline{v}_p \cdot \hat{\mathbf{R}}_S$ in this case (see Appendix A). Correspondingly, the values of σ_{PM} of Table 4 are changed to 18.43 Hz, 55.30 Hz, and 165.88 Hz at VHF, UHF, L-band, respectively. Note that these modified values are still the maximum σ_{PM} achieved over the data.

The selection of 577 Hz and 1 μs for the PRF and compressed pulsewidth correspond to 1733 (N_r) range cells per unambiguous range interval (Eq.(14)). The number of unambiguous range intervals within the mainbeam are given in Table 5. Set 1 corresponds to the data set for which the Wideband boresight pointed nearest the optical horizon ($\phi \simeq 59.425°$). Hence the number of unambiguous range intervals for set 1 is the largest of all the Ancon data. Sets 2 and 3 correspond to the maximum and minimum values of σ_{PM} for the data (Table 4). The last two sets are the minimum (0 Hz,0 Hz,0 Hz) and the maximum (36.98 Hz, 110.93 Hz, 332.79 Hz) values that σ_{PM} can attain for VHF, UHF, and L-band and for an arbitrary, 1030-km orbit.

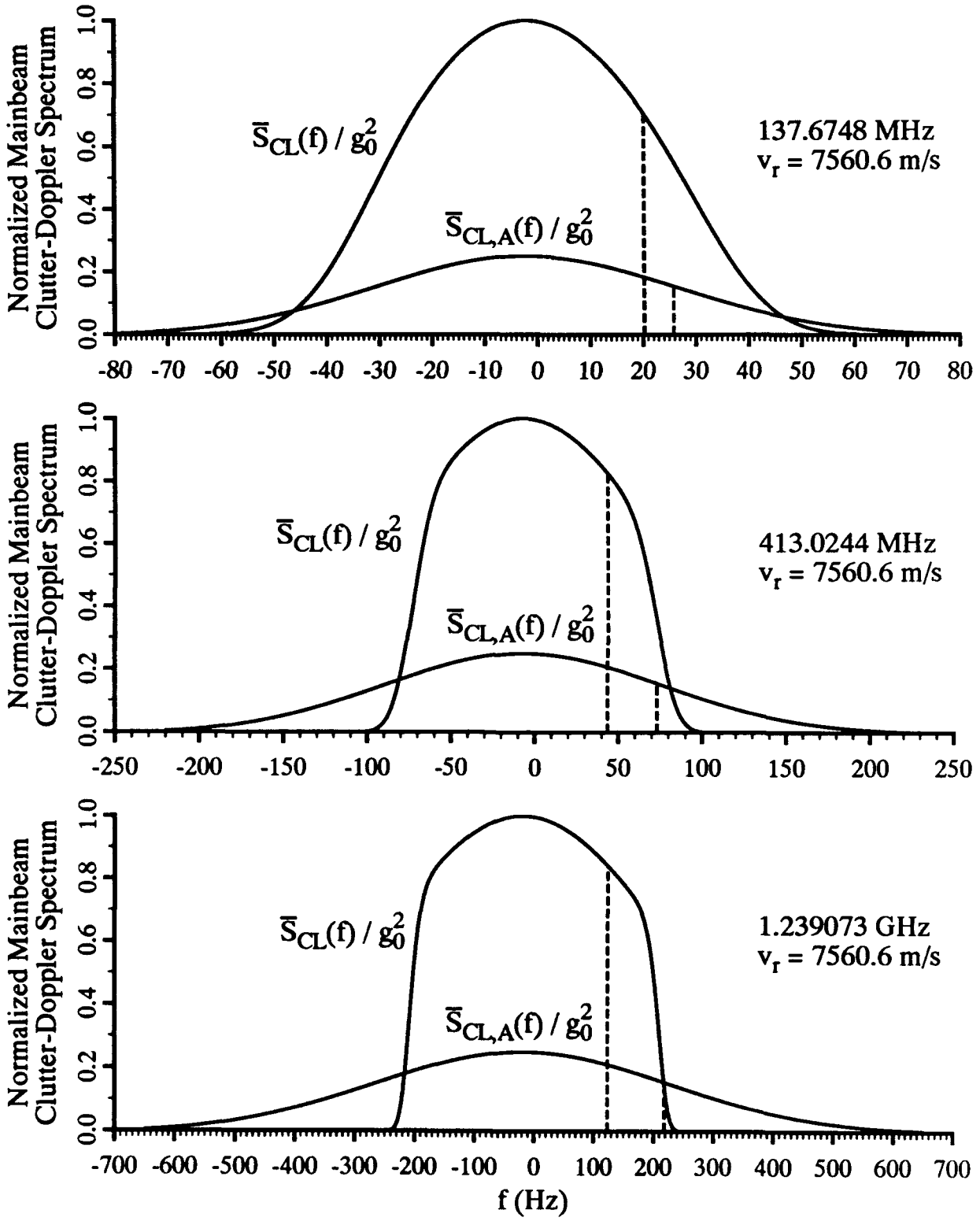

Fig. 8 — Exact and approximate mainbeam clutter-Doppler spectra for set #1 at VHF, UHF, and L-band. Both spectra are normalized to the maximum value of the exact spectrum. Twice the horizontal distance between the frequency of the maximum value of each spectrum and the vertical lines to both curves correspond to the clutter spread for each function.

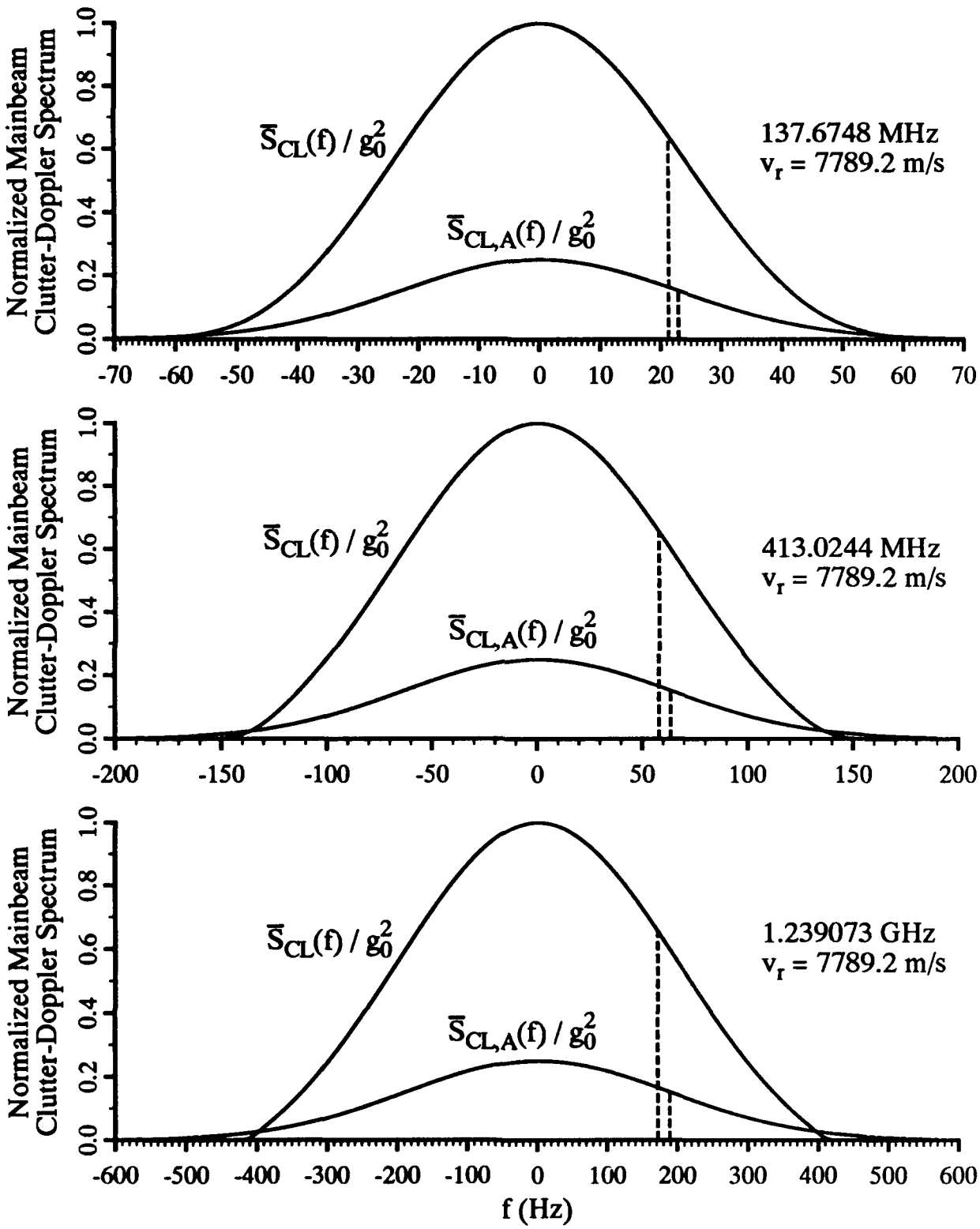

Fig. 9 — Exact and approximate mainbeam clutter-Doppler spectra for set #2 at VHF, UHF, and L-band. Both spectra are normalized to the maximum value of the exact spectrum. Twice the horizontal distance between the frequency of the maximum value of each spectrum and the vertical lines to both curves correspond to the clutter spread for each function.

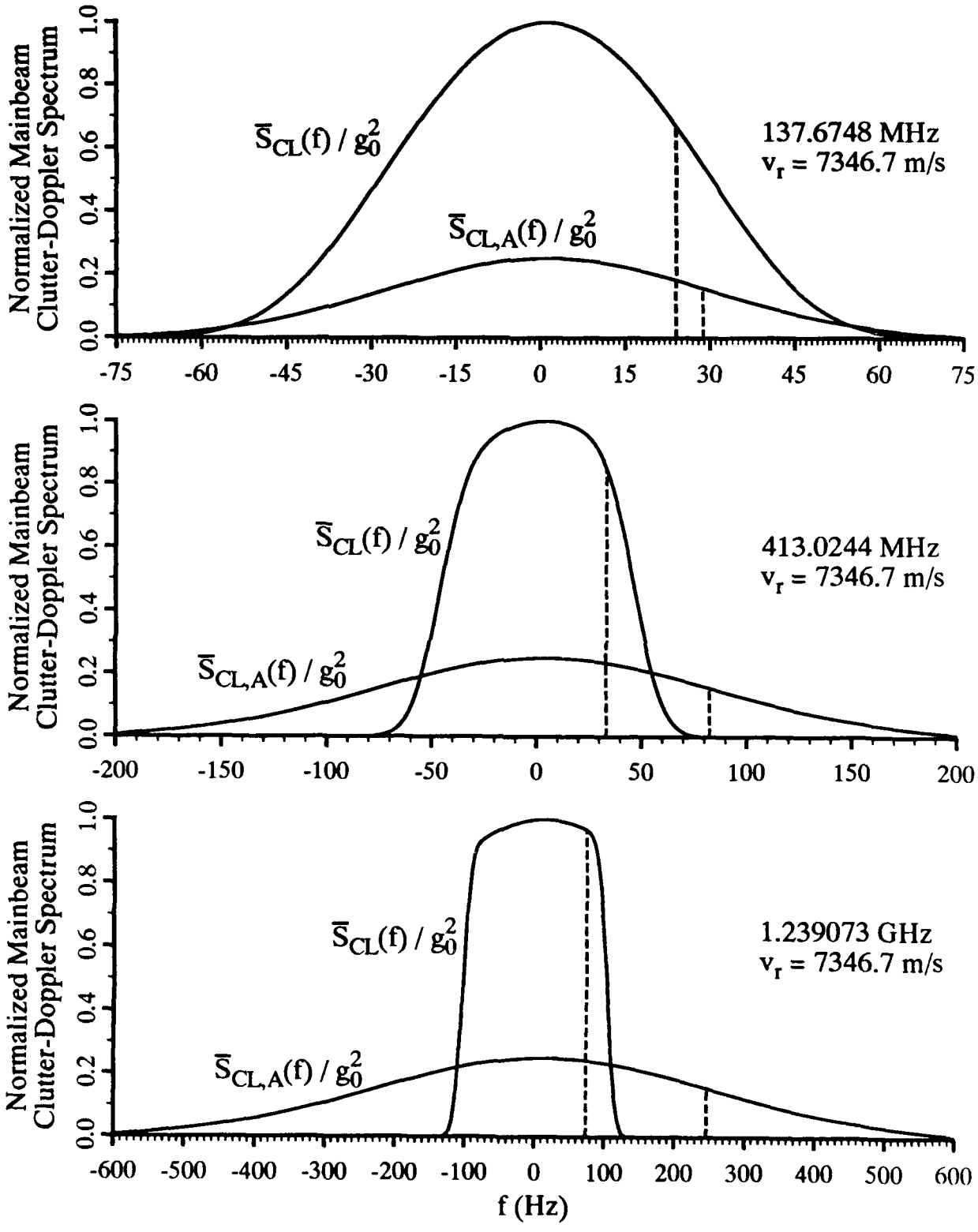

Fig. 10 — Exact and approximate mainbeam clutter-Doppler spectra for set #3 at VHF, UHF, and L-band. Both spectra are normalized to the maximum value of the exact spectrum. Twice the horizontal distance between the frequency of the maximum value of each spectrum and the vertical lines to both curves correspond to the clutter spread for each function.

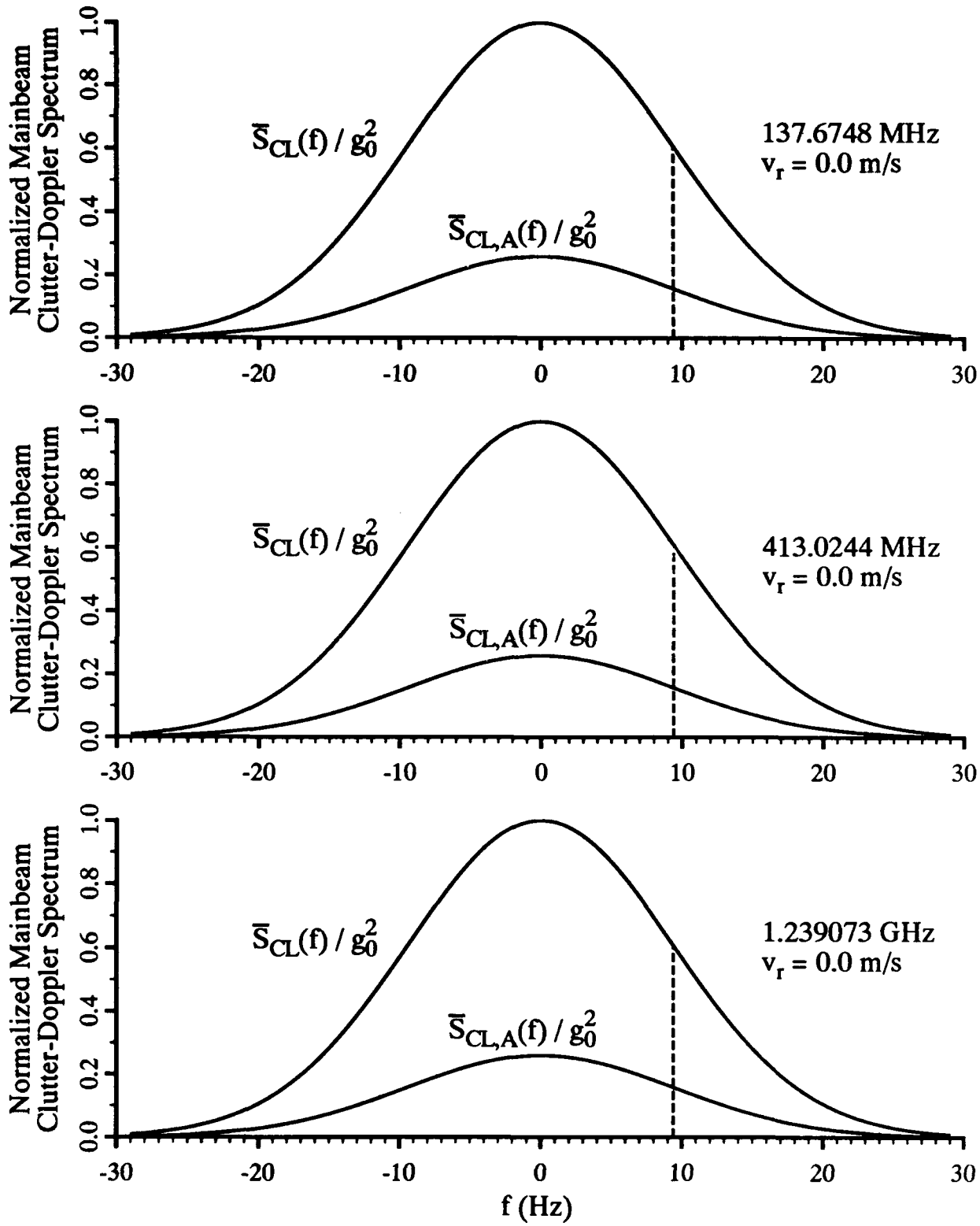

Fig. 11 — Exact and approximate mainbeam clutter-Doppler spectra for set #4 at VHF, UHF, and L-band. Both spectra are normalized to the maximum value of the exact spectrum. Twice the horizontal distance between the frequency of the maximum value of each spectrum and the vertical lines to both curves correspond to the clutter spread for each function.

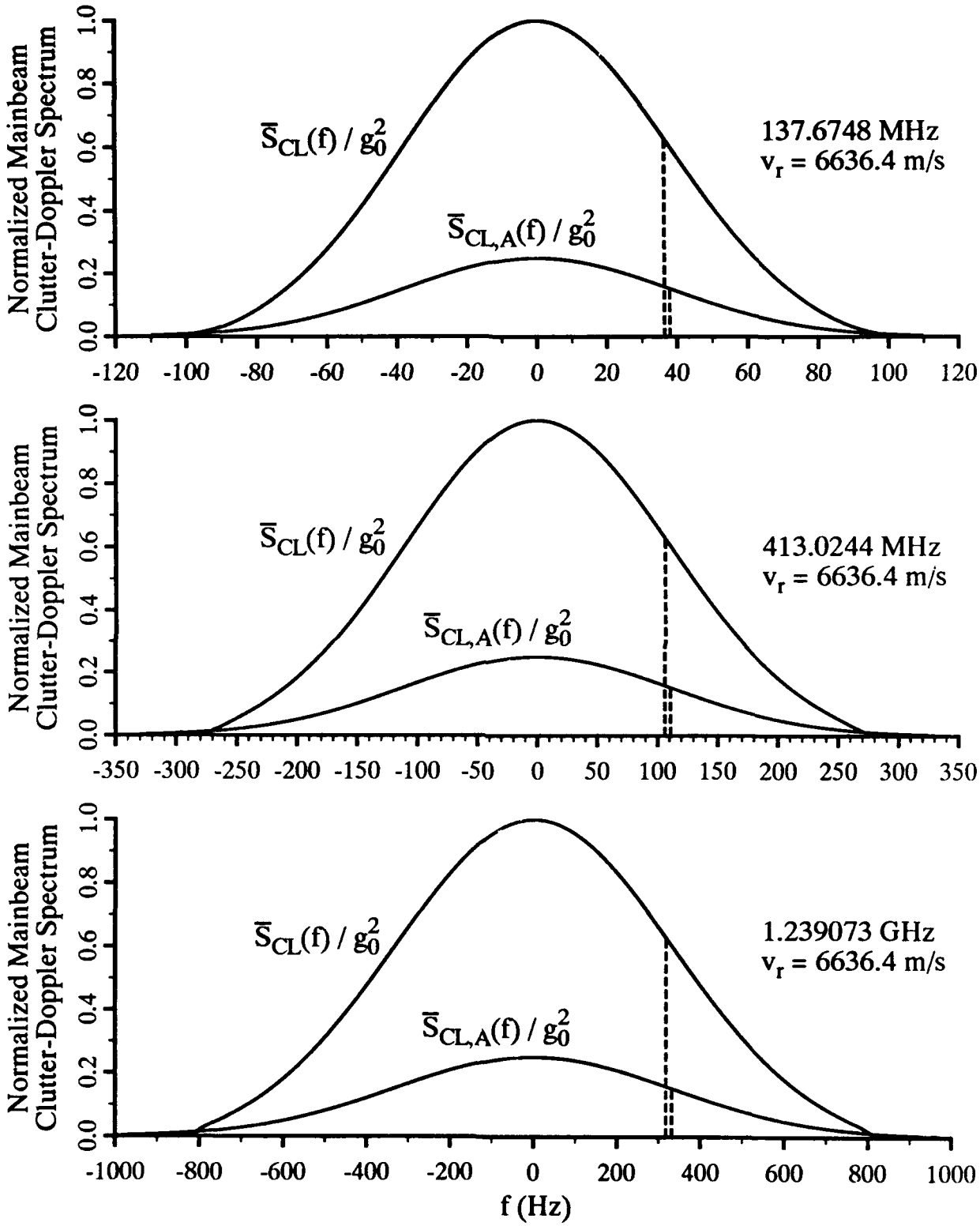

Fig. 12 — Exact and approximate mainbeam clutter-Doppler spectra for set #5 at VHF, UHF, and L-band. Both spectra are normalized to the maximum value of the exact spectrum. Twice the horizontal distance between the frequency of the maximum value of each spectrum and the vertical lines to both curves correspond to the clutter spread for each function.

Table 6 — Clutter-Doppler Spectral Spreads and Maxima

Set	Freq	σ_{PM} (Hz)	σ_{CL} (Hz)	$\bar{\sigma}_{CL}$ (Hz)	$\bar{\sigma}_{CL,A}$ (Hz)	$\arg\{\max(\bar{S}_{CL})\}$ (Hz)	$\max(\bar{S}_{CL})$ ($\times 10^{-18}$)
1	VHF	9.95	13.71	22.39	28.02	-2.123	1.77651
1	UHF	29.85	31.30	50.25	79.83	-6.576	0.62352
1	L-band	89.54	90.03	142.96	238.00	-19.716	0.20909
2	VHF	18.43	20.70	21.25	22.87	0.104	6.41250
2	UHF	55.29	56.09	57.63	63.22	0.316	2.31994
2	L-band	165.88	166.15	171.03	187.87	0.952	0.78098
3	VHF	4.55	10.47	22.85	27.51	1.230	2.34508
3	UHF	13.65	16.59	29.29	78.25	4.010	0.82969
3	L-band	40.94	42.01	61.49	233.60	12.306	0.27828
4	VHF	0.00	9.43	9.48	9.48	0.000	15.06030
4	UHF	0.00	9.43	9.48	9.48	0.000	15.06030
4	L-band	0.00	9.43	9.48	9.48	0.000	15.06030
5	VHF	36.98	38.16	36.42	37.93	0.016	1.31096
5	UHF	110.93	111.33	106.21	110.81	0.000	0.44956
5	L-band	332.79	332.92	317.53	331.54	0.083	0.15034

A natural question is whether the spectra $\bar{S}_{CL}$ and $\bar{S}_{CL,A}$ are Gaussian. These spectra are graphed in Figs. 8 to 12. Let f_M and f_{MA} be the maxima associated with $\bar{S}_{CL}$ and $\bar{S}_{CL,A}$, respectively. Although Gaussian fits to the data are not shown, sets 2 and 5 are nearly Gaussian, set 4 is Gaussian, and sets 1 and 3 are not. Clearly, set 4 is Gaussian because $v_r = 0$; hence the exponential function is identical for every summand of Eq.(25). When normalized, a finite sum of Gaussians of equal standard deviations and zero means is a zero-mean Gaussian with the same standard deviation, evidenced by the fact that $\sigma_{CL} = \bar{\sigma}_{CL}$ in Table 6.

Sets 1 and 3 are also not symmetric about f_M, since more area beneath $\bar{S}_{CL}$ lies to the right of f_M than to the left of it (Figs. 8 and 10). Nonetheless, the standard deviations $\bar{\sigma}_{CL}$ and $\bar{\sigma}_{CL,A}$ are defined to be the frequencies for which the areas under $\bar{S}_{CL}$ and $\bar{S}_{CL,A}$ within the intervals $[f_M, f_M + \bar{\sigma}_{CL}]$ and $[f_{MA}, f_{MA} + \bar{\sigma}_{CL,A}]$ are 0.6826 of the area to the right of f_M and f_{MA}. As the spectra become more symmetric about the maxima, this definition agrees more closely with the distance from the 1-sigma points to the center (maximum) of the fitted Gaussian probability density function. The graphs of the exact spectra are close enough to being symmetric to yield reasonable values for $\bar{\sigma}_{CL}$. Intuitively, one expects the summation of many Gaussians with different means to result in spectral spreading ($\bar{\sigma}_{CL} > \sigma_{CL}$). This is true except for set 5, where $\bar{\sigma}_{CL}$ is underestimated because $\bar{S}_{CL}$ matches a Gaussian until $|f| = 700$ Hz, while the exact spectrum decreases more rapidly to zero than the fitted Gaussian for $|f| \geq 700$ Hz. In addition, the difference between $\bar{\sigma}_{CL}$ and σ_{CL} for $v_r \neq 0$ is more pronounced as the frequency increases.

Observe that the maximum f_M, which is taken as the center of the spectrum $\bar{S}_{CL}$, is not approximately zero in all cases. In particular, the maximum in sets 1 and 3 can be several Hz (as much as 2, 6, and 19 for VHF, UHF, and L-band, respectively) away from 0 Hz. This implies that the TACCAR-like correction (Eq.(7)) to the Doppler shift does not necessarily center the spectrum at 0 Hz. Table 6 also indicates that the maximum value of the spectrum decreases with increasing frequency at a given nonzero v_r.

Upon analyzing columns 5 and 6 of Table 6, it is clear that $\bar{\sigma}_{CL,A}$ is, at best, a reasonable approximation of $\bar{\sigma}_{CL}$ (Sets 2 and 5) for nonzero v_r. In fact, the difference, $\bar{\sigma}_{CL,A} - \bar{\sigma}_{CL}$, is nonnegative in all instances, increases with frequency, is substantial for sets 1 and 3, and is zero

for set 4 (since $B = 0$). Therefore, unless v_r is small enough, the representation of the spectrum given by Eqs.(31) and (32) should be used.

Recall that $\sigma_{IN}(v)$ is 1 m/s and σ_{SC} is 9.38 Hz. Since $\sigma(f) = 2f_t\sigma(v)/c$ relates the frequency- and velocity-dependent spreads, $\sigma_{IN}(f)$ is 0.92 Hz, 2.76 Hz, and 8.27 Hz at VHF, UHF, and L-band, respectively. Depending on the antenna's position in a 1030-km orbit, σ_{PM} ranges from 0 Hz to 369 Hz. Clearly, $\sigma_{IN} < \sigma_{SC}$ for these calculations. At VHF, $\sigma_{SC} \gg \sigma_{IN}$ and σ_{IN} contributes very little to σ_{CL} in the absence of σ_{PM}. However, as the frequency increases to L-band, σ_{IN} and σ_{SC} are nearly the same and contribute almost equally to σ_{CL} when $\sigma_{PM} \simeq 0$. On the other hand, σ_{PM} can be large compared to σ_{SC} and σ_{IN}, in which case $\sigma_{PM} \simeq \sigma_{CL}$.

As indicated previously, one expects spectral spreading from integration over the antenna's mainbeam; that is, $\bar{\sigma}_{CL}$ is larger than σ_{CL}. The spreading is a minimum ($\bar{\sigma}_{CL} - \sigma_{CL} = 0.0538$ Hz) when σ_{PM} is zero and increases with frequency, except for the noted aberration of set 5.

5.0 SUMMARY

Two expressions for the clutter-Doppler spectrum within a range cell and for the total spectrum over a narrow, Gaussian mainlobe are derived for an SBR. These expressions are applicable to an SBR in a 1030-km orbit with a carrier frequency between 100 MHz and 1300 MHz during severe ionospheric conditions. In all situations, it is more desirable to use the more exact of the two expressions, except when the speed of the satellite relative to the speed of the surface clutter patch is "near" zero. The depth of this study is insufficient to determine a quantitative definition of nearness.

A total spectrum is not necessarily symmetric about its maximum; however, each spectrum is sufficiently symmetric to define a center (maximum) and a spread about the maximum that are analogous to the mean and standard deviation of a Gaussian probability density function. At VHF, UHF, and L-band, the center of the mainbeam's spectrum can be offset from zero by as much as 2.12, 6.58, and 19.72 Hz, respectively. Since these calculations include a TACCAR-like correction to the Doppler shift, such a correction does not compensate completely for the translation of the spectrum caused by platform motion. If the offsets from 0 Hz are significant to an SBR system, then an additional correction is required to center the spectrum at zero; however, making this correction is limited by the ability to perform such signal processing.

Calculations of σ_{SC}, σ_{CL}, and $\bar{\sigma}_{CL}$ are made for the minimum value of τ_0 (24 ms) over the Wideband data collected at Ancon (Peru) from 22 satellite passes in 1977. This minimum value is typical of severe scintillation conditions and yields a σ_{SC} of 9.38 Hz. For the data, the intrinsic clutter-Doppler spread σ_{IN} ranges from 0.92 Hz to 8.27 Hz. Depending on the orbital position, σ_{PM} takes on values between 0 Hz and 369 Hz. When σ_{PM} is near zero and σ_{IN} is small compared to σ_{SC}, for example at VHF, $\sigma_{CL} \simeq \sigma_{SC}$. Situations also exist where σ_{SC} and σ_{IN} are comparable for small σ_{PM}. On the other hand, as σ_{PM} increases, it dominates σ_{SC} and σ_{IN} so that $\sigma_{CL} \simeq \sigma_{PM}$. All of these situations occur or can occur for a satellite in some 1030-km orbit. Thus, in some cases, eliminating the clutter-Doppler spread caused by platform motion with techniques like DPCA result in a negligible decrease in the spectral spreads, whereas in other instances, the decrease is dramatic. At best, one can reduce σ_{CL} and $\bar{\sigma}_{CL}$ only to $\sqrt{\sigma_{IN}^2 + \sigma_{SC}^2} \simeq 9.43$ Hz and 9.48 Hz, respectively, in severe scintillation. The preceding two limits provide lower bounds on the achievable reduction in clutter-Doppler spread. To obtain a more quantitative idea of the ramifications of these bounds, one must implement a system architecture and analyze improvement factors, clutter cancelers, and the like.

6.0 ACKNOWLEDGEMENTS

The author gratefully acknowledges the help of Dr. J. A. Eisele for running his computer program (FOPP8) and for providing invaluable data and counsel on satellite orbitology; Mr. B. T. Smith for performing the computer work necessary to the analysis and figures contained herein; Dr. K. Gerlach for the enlightening discussions on the clutter-Doppler spectrum; and Dr. G. A. Andrews for reviewing the manuscript.

7.0 REFERENCES

Aerospace Defense Command/Space Computational Center Program Documentation ADCOM DCD 8, "Mathematical Foundation for SCC Astrodynamic Theory," 1977.

G. A. Andrews, Jr., "Airborne Radar Motion Compensation Techniques: Optimum Array Correction Patterns," NRL Report 7977, Mar. 1976.

G. A. Andrews, "Radar Antenna Pattern Design for Platform Motion," *IEEE Trans. Ant. Propag.* **AP-26**(4), 566–571 (1978).

G. A. Andrews and K. Gerlach, "SBR Clutter and Interference," in *Space-Based Radar Handbook*, L. J. Cantafio, ed. (Artech House, Norwood MA, 1989), Ch. 11.

R. R. Bate, D. D. Mueller, and J. E. White, *Fundamentals of Astrodynamics* (Dover Publications, Inc., New York, 1971), p. 103.

J. A. Eisele and P. E. V. Shannon, "User Oriented Fast Orbit Prediction Program," NRL Memorandum Report 3105, Sept. 1975.

E. J. Fremouw, R. L. Leadabrand, R. C. Livingston, M. D. Cousins, C. L. Rino, B. C. Fair, and R. A. Long, "Early Results from the DNA Wideband Satellite Experiment," *Radio Sci.* **13**, 167–187 (1978).

D. G. King-Hele, J. A. Pilkington, D. M. Walker, H. Hiller, and A. N. Winterbottom, *The RAE Table of Earth Satellites 1957–1986* (Stockton Press, New York, 1988), p. 447.

D. L. Knepp and R. A. Dana, "The Impact of Strong Scintillation on Space-Based Radar Design: Clutter Rejection," *Radio Sci.* **20**, 366–374 (1985).

D. L. Knepp and E. L. Mokole, "Space-Based Radar Coherent Processing during Scintillation: VHF through L-band," submitted to *Radio Sci.*

E. L. Mokole and D. L. Knepp, "Integration Losses for a Two-Way, Transionospheric, Propagation Path Caused by Ionospheric Scintillation," submitted to *IEEE Trans. Aero. Elec. Sys.*

W. W. Shrader and V. Gregers-Hansen, "MTI Radar," in *Radar Handbook*, 2nd ed., M. Skolnik, ed. (McGraw-Hill, New York, 1990), Ch. 15.

Appendix A
APPROXIMATION OF THE DOPPLER SHIFT

The Doppler shift of a scatterer at point P_S in the direction $\hat{\mathbf{R}}_S$ is

$$f_D = \frac{2f_t}{c}(\underline{v}_r \cdot \hat{\mathbf{R}}_S),$$

where $\underline{v}_r = \underline{v}_p - \underline{v}_e$. Two approximations can be made in Eq.(4): replacement of $\underline{v}_r \cdot \hat{\mathbf{R}}_S$ with $\underline{v}_p \cdot \hat{\mathbf{R}}_S$ or γ_r with γ_S. This appendix addresses the accuracy of these replacements for a circular orbit at 1030 km.

The speed of the rotating point P_S is

$$\begin{aligned} v_e &= |\underline{v}_e| = |\underline{w} \times \underline{r}_g| = |(\omega_e \underline{K}) \times \underline{r}_g| \\ &= \left|\omega_e(-r_{gY}\underline{I} + r_{gX}\underline{J})\right| = \omega_e\sqrt{r_{gX}^2 + r_{gY}^2} = \omega_e R_e\left|\cos L\right|, \end{aligned} \tag{A1}$$

where

$$\begin{aligned} \omega_e &= \frac{\pi}{(12)(3600)}\frac{\text{rad}}{\text{s}}, \\ r_{gX} &= R_e \cos L \cos \xi, \\ r_{gY} &= R_e \cos L \sin \xi. \end{aligned} \tag{A2}$$

The angles L and ξ are the latitude and longitude, respectively, of the ground station (see Fig. 1(c)), and R_e (6378.145 km) is the radius of the Earth. Therefore, $v_e = \omega_e R_e \cos L$, which is independent of the longitude of the ground station. For the site at Ancon, Peru, the latitude is -11.767°. Hence $v_e \simeq 454.0843718$ m/s.

According to (Eisele and Nichols 1976, p.12), the orbital speed of a satellite in m/s is

$$v_p \simeq (4.2685)(1852)\sqrt{\frac{R_e}{R_e + h}} \simeq 7335.145367\,\frac{\text{m}}{\text{s}}, \tag{A3}$$

where h (1030 km) is the satellite's altitude.

Comparing the two speeds yields $v_e \simeq 0.0619053\,v_p$; that is, v_e is about 6.19% of v_p for a 1030-km orbit. Thus for $\cos\gamma_S \neq 0$,

$$\begin{aligned} \underline{v}_r \cdot \hat{\mathbf{R}}_S &= \underline{v}_p \cdot \hat{\mathbf{R}}_S - \underline{v}_e \cdot \hat{\mathbf{R}}_S \\ &\simeq v_p\left[\cos\gamma_S - 0.0619053\cos\psi_{eS}\right] \\ &\simeq \left[\underline{v}_p \cdot \hat{\mathbf{R}}_S\right]\left[1 - 0.0619053\frac{\cos\psi_{eS}}{\cos\gamma_S}\right] \\ &= D\left[\underline{v}_p \cdot \hat{\mathbf{R}}_S\right], \end{aligned} \tag{A4}$$

where γ_S and ψ_{eS} are the angles between v_p and $\underline{R}_S$ and v_e and $\underline{R}_S$, respectively. The constant D is the second bracketed expression in the next to last line of Eq.(A4). Whether the term

$$0.0619053\frac{\cos\psi_{eS}}{\cos\gamma_S} \tag{A5}$$

can be neglected depends on the satellite's orbit and the direction of antenna's boresight. When the magnitude of this expression is large (> 0.1), $\underline{v}_r \cdot \hat{\mathbf{R}}_S$ *cannot* be accurately approximated by $\underline{v}_p \cdot \hat{\mathbf{R}}_S$. For example, if γ_S is near $\pi/2$ and ψ_{eS} is not, then this quantity gets very large. In fact, it approaches infinity. If $\theta_S = \pi/2, 3\pi/2$ (near broadside) or $\phi_S = 0$ (nadir), then $\underline{v}_r \cdot \hat{\mathbf{R}}_S = -\underline{v}_e \cdot \hat{\mathbf{R}}_S$. Therefore, the component of f_D from the platform speed is zero, when the mainbeam points broadside or in the nadir direction.

At the equator, $\underline{v}_e$ is perpendicular to the nadir direction and points along the equator. Analysis of the geometry leads to

$$\frac{\pi}{2} - \arcsin\left(\frac{R_e}{R_e + h}\right) \leq \psi_{eS} \leq \frac{\pi}{2} + \arcsin\left(\frac{R_e}{R_e + h}\right) \tag{A6}$$

or

$$-\frac{R_e}{R_e + h} \leq \cos\psi_{eS} \leq \frac{R_e}{R_e + h} \tag{A7}$$

for radars that only look out to the optical horizon.

To determine the values of D for the Wideband data, ψ_{eS} must be expressed in terms of measurable quantities. The radar site measures the position $\underline{\rho}$ of the satellite relative to the site's position in topocentric coordinates. In Fig. 1, $\underline{\rho}$ corresponds to $-\underline{\mathbf{R}}_S$. In particular,

$$\underline{\rho} = \rho_S \underline{\mathrm{S}} + \rho_E \underline{\mathrm{E}} + \rho_Z \underline{\mathrm{Z}}, \tag{A8}$$

where

$$\begin{aligned} \rho_S &= -\rho \cos El \cos Az, \\ \rho_E &= \rho \cos El \sin Az, \\ \rho_Z &= \rho \sin El. \end{aligned} \tag{A9}$$

Therefore,

$$\hat{\mathbf{R}}_S = (\cos El \cos Az)\underline{\mathrm{S}} + (-\cos El \sin Az)\underline{\mathrm{E}} + (-\sin El)\underline{\mathrm{Z}} \tag{A10}$$

and

$$\underline{v}_e \cdot \hat{\mathbf{R}}_S = (v_e \underline{\mathrm{E}}) \cdot \hat{\mathbf{R}}_S = v_e \cos\psi_{eS}. \tag{A11}$$

Combining Eqs. (A10) and (A11) yields

$$\cos\psi_{eS} = -\cos El \sin Az. \tag{A12}$$

Therefore,

$$D = 1 + 0.0619053 \frac{\cos El \sin Az}{\cos\theta_S \sin\phi_S}. \tag{A13}$$

To use the Wideband data, set $\phi_S = \phi_a$ and $\theta_S = \theta_a$. Since El, Az, ϕ_a, and θ_a are measured and tabulated in Table 2, the values of D and the absolute error, $|(D-1)/D|$, are computed in Table A1. The error is good only for the last three rows of Table A1 and is less than 10% for all but one the data sets, where it is a substantial 23.77%. Unfortunately, this is one of the sets analyzed in Table 5. In fact, the errors are 2.87%, 3.89%, and 23.77% for Sets 1, 2, and 3, respectively, of Table 5.

Table A1 — Values of D and the Absolute Error for an Orbit Relative to Ancon

Az (Deg)	El (Deg)	ϕ_a (Deg)	θ_a (Deg)	D	Absolute Error (%)
23.6	10.4	58.297	346.34	1.0295	2.87
25.5	15.8	56.503	344.68	1.0319	3.09
28.1	22.4	53.516	342.25	1.0352	3.40
32.3	30.9	48.752	338.48	1.0405	3.89
39.8	42.0	41.427	331.68	1.0506	4.82
56.1	55.7	31.188	317.52	1.0758	7.05
96.6	65.8	21.731	282.61	1.3119	23.77
124.1	64.7	24.411	232.50	0.9129	9.54
157.9	52.8	35.007	207.69	0.9723	2.85
171.3	39.7	44.066	197.24	0.9892	1.09
177.8	29.3	50.231	191.86	0.9972	0.28
-178.5	21.4	54.182	188.64	1.0019	0.19
-176.2	15.1	56.632	186.50	1.0048	0.48

To avoid approximations to the Doppler shift, exact expressions must be employed when analyzing $\underline{v}_r \cdot \hat{\mathbf{R}}_S$. One major approximation, which greatly simplifies the analysis, is substituting γ_S for γ_r. To obtain γ_r exactly, express $\underline{R}_S$ and $\underline{v}_r$ in the vehicle-centered frame (x, y, z):

$$\underline{R}_S = x_S\underline{x} + y_S\underline{y} + z_S\underline{z} \qquad \text{and} \qquad \underline{v}_r = v_{rx}\underline{x} + v_{ry}\underline{y} + v_{rz}\underline{z},$$

where

$$\begin{aligned} x_S &= R_S \cos\theta_S \sin\phi_S & & & v_{rx} &= v_r \cos\theta_r \sin\phi_r \\ y_S &= R_S \sin\theta_S \sin\phi_S & & \text{and} & v_{ry} &= v_r \sin\theta_r \sin\phi_r \\ z_S &= R_S \cos\phi_S & & & v_{rz} &= v_r \cos\phi_r. \end{aligned}$$

Equating both sides of

$$v_r \cos\gamma_r = \underline{v}_r \cdot \hat{\mathbf{R}}_S = \frac{1}{R_S}(v_{rx}x_S + v_{ry}y_S + v_{rz}z_S)$$

leads to

$$\cos\gamma_r = \cos\theta_r \sin\phi_r \cos\theta_S \sin\phi_S + \sin\theta_r \sin\phi_r \sin\theta_S \sin\phi_S + \cos\phi_r \cos\phi_S. \tag{A14}$$

The computation of ϕ_r and θ_r requires precise information about both the position and the velocity of the satellite with respect to the three coordinate frames that are mentioned in Sections 1 and 2.

Lastly, one more expression for $\underline{v}_r \cdot \hat{\mathbf{R}}_S$ is derived. By Eqs.(A8) and (A9),

$$\dot{\underline{\rho}} = \dot{\rho}_S\underline{S} + \dot{\rho}_E\underline{E} + \dot{\rho}_Z\underline{Z}, \tag{A15}$$

where

$$\begin{aligned} \dot{\rho}_S &= -\dot{\rho}\cos El \cos Az + \rho\dot{El}\sin El \cos Az + \rho\dot{Az}\cos El \sin Az, \\ \dot{\rho}_E &= \dot{\rho}\cos El \sin Az - \rho\dot{El}\sin El \sin Az + \rho\dot{Az}\cos El \cos Az, \\ \dot{\rho}_Z &= \dot{\rho}\sin El + \rho\dot{El}\cos El. \end{aligned} \tag{A16}$$

Since $\underline{v}_r = \dot{\underline{\rho}}$,

$$\underline{v}_r \cdot \hat{\mathbf{R}}_S = \dot{\underline{\rho}} \cdot \left(\frac{-\underline{\rho}}{\rho}\right) = \frac{-1}{\rho}(\dot{\rho}_S\underline{S} + \dot{\rho}_E\underline{E} + \dot{\rho}_Z\underline{Z}) = -\dot{\rho} = \dot{R}_S, \tag{A17}$$

after some algebra. When applying the Wideband data, $\dot{R}_S = \dot{R}_a$.

REFERENCE

J. A. Eisele and S. A. Nichols, "Orbital Mechanics of General-Coverage Satellites," NRL Report 7975, Apr. 1976.

Appendix B
APPROXIMATION OF AVERAGE DOPPLER OVER NARROW MAINBEAMS

An approximate expression for the average Doppler over a narrow mainbeam is derived for isotropic, homogeneous clutter. By Eq.(5),

$$\bar{f}_D = \frac{1}{\text{Area}(\mathcal{A})} \iint_{\mathcal{A}} f_D(r,\phi,\theta)\, d\mathcal{A} \simeq \frac{\iint_{\Omega} f_D(R_0,\phi,\theta) R_0^2 \sin\phi \, d\phi d\theta}{\iint_{\Omega} R_0^2 \sin\phi \, d\phi d\theta}. \tag{B1}$$

Assuming that v_r is essentially constant over Ω and substituting $f_D(R_0,\phi,\theta) = (2f_t v_r/c)\sin\phi\cos\theta$ into Eq.(B1) yields

$$\bar{f}_D \simeq \frac{2f_t v_r}{c} \frac{\iint_{\Omega} \cos\theta \sin^2\phi \, d\phi d\theta}{\iint_{\Omega} \sin\phi \, d\phi d\theta}, \tag{B2}$$

where ϕ and θ run over all scatterers in the mainbeam and the subscript S of Eq.(4) is dropped.

The geometry of Ω clearly determines the evaluation of Eq.(B2). However, for narrow mainbeams, the right side of Eq.(B2) reduces to the same approximate formula for small (ϵ and δ are small) rectangular (Ω_1) and elliptical (Ω_2) neighborhoods about (ϕ_a, θ_a):

$$\begin{aligned} \Omega_1 &= \Big\{(\phi,\theta) : \phi_a - \epsilon \le \phi \le \phi_a + \epsilon \quad \& \quad \theta_a - \delta \le \theta \le \theta_a + \delta\Big\}, \\ \Omega_2 &= \Big\{(\phi,\theta) : \Big(\frac{\phi-\phi_a}{\epsilon}\Big)^2 + \Big(\frac{\theta-\theta_a}{\delta}\Big)^2 \le 1\Big\}. \end{aligned} \tag{B3}$$

Since evaluation of the integrals over Ω_1 in Eq.(B2) is straightforward, the approximation is derived for Ω_2. With the change of variables from (ϕ,θ) to (u,v),

$$\begin{aligned} \phi &= \epsilon u \cos v + \phi_a \\ \theta &= \delta u \sin v + \theta_a, \end{aligned} \tag{B4}$$

Ω_2 and the areal element $d\phi d\theta$ become $\{(u,v) : 0 \le u \le 1 \quad \& \quad 0 \le v \le 2\pi\}$ and $\epsilon\delta u\, du dv$, respectively.

First, consider the integral in the numerator of Eq.(B2).

$$\iint_{\Omega_2} \cos\theta \sin^2\phi \, d\phi d\theta = \frac{\epsilon\delta}{2} \int_0^{2\pi} \int_0^1 u \Big\{\cos(u\delta \sin v + \theta_a)\Big[1 - \cos(2u\epsilon\cos v + 2\phi_a)\Big]\Big\} du dv. \tag{B5}$$

In the two terms of the inner integral, use trigonometric identities, integrate by parts, and apply

the small-angle approximations, $\sin z \simeq z$ and $\cos z \simeq 1$, to obtain

$$\int_0^1 u\cos(u\delta\sin v+\theta_a)\cos(2u\epsilon\cos v+2\phi_a)\,du = \frac{1}{2}\int_0^1 u\Big\{\cos\big[u(\delta\sin v-2\epsilon\cos v)+(\theta_a-2\phi_a)\big] + \cos\big[u(\delta\sin v+2\epsilon\cos v)+(\theta_a+2\phi_a)\big]\Big\}\,du$$

$$= \frac{1}{2}\Bigg\{u\Bigg(\frac{\sin\big[u(\delta\sin v-2\epsilon\cos v)+(\theta_a-2\phi_a)\big]}{\delta\sin v-2\epsilon\cos v} + \frac{\sin\big[u(\delta\sin v+2\epsilon\cos v)+(\theta_a+2\phi_a)\big]}{\delta\sin v+2\epsilon\cos v}\Bigg) + \frac{\cos\big[u(\delta\sin v-2\epsilon\cos v)+(\theta_a-2\phi_a)\big]}{(\delta\sin v-2\epsilon\cos v)^2} + \frac{\cos\big[u(\delta\sin v+2\epsilon\cos v)+(\theta_a+2\phi_a)\big]}{(\delta\sin v+2\epsilon\cos v)^2}\Bigg\}\Bigg|_0^1$$

$$\simeq \frac{1}{2}\Bigg\{\frac{(\delta\sin v-2\epsilon\cos v)\cos(\theta_a-2\phi_a)+\sin(\theta_a-2\phi_a)}{\delta\sin v-2\epsilon\cos v} + \frac{(\delta\sin v+2\epsilon\cos v)\cos(\theta_a+2\phi_a)+\sin(\theta_a+2\phi_a)}{\delta\sin v+2\epsilon\cos v} - \frac{\sin(\theta_a-2\phi_a)}{\delta\sin v-2\epsilon\cos v} - \frac{\sin(\theta_a+2\phi_a)}{\delta\sin v+2\epsilon\cos v}\Bigg\}$$

$$= \cos\theta_a\cos(2\phi_a). \tag{B6}$$

Similar manipulations lead to

$$\int_0^1 u\cos(u\delta\sin v+\theta_a)\,du \simeq \cos\theta_a. \tag{B7}$$

Substituting Eqs.(B6) and (B7) into Eq.(B5) yields

$$\iint_{\Omega_2}\cos\theta\sin^2\phi\,d\phi d\theta \simeq \frac{\epsilon\delta}{2}\int_0^{2\pi}\cos\theta_a\big[1-\cos(2\phi_a)\big]\,dv$$

$$= 2\pi\epsilon\delta\cos\theta_a\sin^2\phi_a. \tag{B8}$$

Evaluation of the denominator of Eq.(B2) is much simpler; that is,

$$\iint_{\Omega_2}\sin\phi\,d\phi d\theta = \epsilon\delta\int_0^{2\pi}\int_0^1 u\sin(\epsilon u\cos v+\phi_a)\,du dv$$

$$= \epsilon\delta\int_0^{2\pi}\Bigg\{-\frac{u\cos(\epsilon u\cos v+\phi_a)}{\epsilon\cos v}+\frac{\sin(\epsilon u\cos v+\phi_a)}{(\epsilon\cos v)^2}\Bigg\}\Bigg|_0^1 dv$$

$$\simeq \epsilon\delta\int_0^{2\pi}\sin\phi_a\,dv = 2\pi\epsilon\delta\sin\phi_a. \tag{B9}$$

Combining Eqs.(B2), (B8), (B9) yields the desired result,

$$\bar{f}_D \simeq \frac{2f_t v_r}{c}\cos\theta_a\sin\phi_a. \tag{B10}$$

Appendix C
RESIDUAL DOPPLER

By Eqs.(7) and (23),

$$F'_D\left(\bar{\phi}_{mn},\bar{\theta}\right) = f'_D\left(\bar{\phi}_{mn}+\phi_a,\bar{\theta}+\theta_a\right) = \frac{2f_t v_r}{c}\left\{\cos(\bar{\theta}+\theta_a)\sin(\bar{\phi}_{mn}+\phi_a) - \cos\theta_a \sin\phi_a\right\}$$
$$= \frac{2f_t v_r}{c}\left\{\cos\bar{\theta}\sin\bar{\phi}_{mn}\cos\theta_a\cos\phi_a + \cos\bar{\theta}\cos\bar{\phi}_{mn}\cos\theta_a\sin\phi_a\right.$$
$$\left. - \sin\bar{\theta}\sin\bar{\phi}_{mn}\sin\theta_a\cos\phi_a - \sin\bar{\theta}\cos\bar{\phi}_{mn}\sin\theta_a\sin\phi_a - \cos\theta_a\sin\phi_a\right\}. \qquad \text{(C1)}$$

Suppose the mainbeam is narrow; that is, $\bar{\theta}$ and $\bar{\phi}_{mn}$ are less than or equal to 2°. A first-order approximation to F'_D is obtained by keeping only first-degree terms of $\bar{\theta}$ and $\bar{\phi}_{mn}$ in the products of the Maclaurin expansions of the trigonometric functions that depend on them. In particular,

$$\begin{aligned}
\cos\bar{\theta}\sin\bar{\phi}_{mn} &\simeq \bar{\phi}_{mn},\\
\cos\bar{\theta}\cos\bar{\phi}_{mn} &\simeq 1,\\
\sin\bar{\theta}\sin\bar{\phi}_{mn} &\simeq 0,\\
\sin\bar{\theta}\cos\bar{\phi}_{mn} &\simeq \bar{\theta}.
\end{aligned} \qquad \text{(C2)}$$

Hence

$$F'_D\left(\bar{\phi}_{mn},\bar{\theta}\right) \simeq \frac{2f_t v_r}{c}\left\{\bar{\phi}_{mn}\cos\theta_a\cos\phi_a - \bar{\theta}\sin\theta_a\sin\phi_a\right\}. \qquad \text{(C3)}$$

Appendix D
INTEGRALS INVOLVING THE ANTENNA POWER GAIN

Two points are discussed in this appendix. First, the relationship $\eta = p_0\sqrt{8/\ln(20)}$ is established. Second, the accuracy of replacing Eq.(31) by Eq.(34) is analyzed.

The mainlobe of the Gaussian gain of Eq.(31) is identified with the angle p_0, where $2p_0$ is the mainlobe's beamwidth (Fig. D1). The selection of p_0 depends on the desired beamwidth. This report assumes that 95% of the power lies within the region $Z = \left\{(\bar{\phi},\bar{\theta}) \ : 0 \le \bar{\phi}^2 + \bar{\theta}^2 \ \le p_0^2\right\}$. This implies that

$$\iint_Z \left|\mathcal{G}(\bar{\phi},\bar{\theta})\right|^4 d\bar{\phi}d\bar{\theta} = 0.95 \iint_{\mathbf{R}^2} \left|\mathcal{G}(\bar{\phi},\bar{\theta})\right|^4 d\bar{\phi}d\bar{\theta}.$$

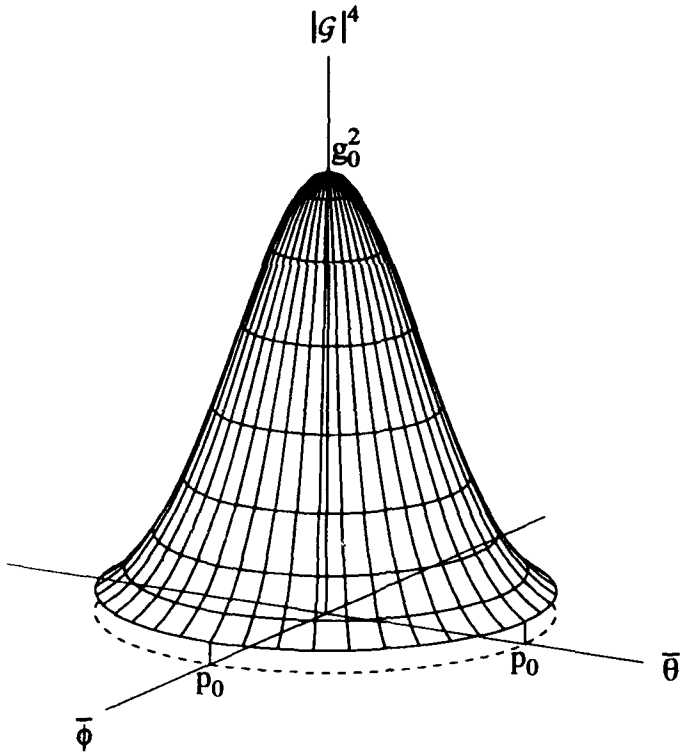

Fig. D1 — The mainlobe of the two-way gain of a Gaussian antenna pattern

With the change of variable $\bar{\phi} = p\cos\delta$ and $\bar{\theta} = p\sin\delta$, the preceding equation becomes

$$\int_0^{2\pi} g_0^2 e^{-8p^2/\eta^2} p\, dp d\delta = 0.95 \int_0^{\infty} g_0^2 e^{-8p^2/\eta^2} p\, dp d\delta,$$

or equivalently,

$$\eta = p_0\sqrt{\frac{8}{\ln(20)}} = p_0\mu, \tag{D1}$$

where $\mu \simeq 0.611936708$.

Next, consider the integral of Eq.(29),

$$\int_{\vartheta^l_{mn}}^{\vartheta^u_{mn}} \left|\mathcal{G}(\bar{\phi}_{mn},\bar{\theta})\right|^4 \exp\left(-\frac{\left(f - F'_D(\bar{\phi}_{mn},\bar{\theta})\right)^2}{2(\sigma^2_{IN}+\sigma^2_{SC})}\right) d\bar{\theta}. \tag{D2}$$

Since the integrand is bounded above by $|\mathcal{G}|^4$, the integral in Eq.(D2) has an upper bound that is the integral of $|\mathcal{G}|^4$ over the same range of integration. Therefore, if

$$\int_{\vartheta^l_{mn}}^{\vartheta^u_{mn}} \left|\mathcal{G}(\bar{\phi}_{mn},\bar{\theta})\right|^4 d\bar{\theta} \simeq \int_{-\infty}^{\infty} \left|\mathcal{G}(\bar{\phi}_{mn},\bar{\theta})\right|^4 d\bar{\theta}, \tag{D3}$$

then

$$\int_{\vartheta^l_{mn}}^{\vartheta^u_{mn}} \left|\mathcal{G}(\bar{\phi}_{mn},\bar{\theta})\right|^4 \exp\left(-\frac{\left(f - F'_D(\bar{\phi}_{mn},\bar{\theta})\right)^2}{2(\sigma^2_{IN}+\sigma^2_{SC})}\right) d\bar{\theta} \simeq \int_{-\infty}^{\infty} \left|\mathcal{G}(\bar{\phi}_{mn},\bar{\theta})\right|^4 \times \exp\left(-\frac{\left(f - F'_D(\bar{\phi}_{mn},\bar{\theta})\right)^2}{2(\sigma^2_{IN}+\sigma^2_{SC})}\right) d\bar{\theta}.$$

By Eq.(30) and $\vartheta^l_{mn} = -\vartheta^u_{mn}$,

$$\int_{\vartheta^l_{mn}}^{\vartheta^u_{mn}} \left|\mathcal{G}(\bar{\phi}_{mn},\bar{\theta})\right|^4 d\bar{\theta} = g_0^2\frac{\eta}{4}\sqrt{2\pi}e^{-8\bar{\phi}^2_{mn}/\eta^2}\left\{2P\left(\frac{4}{\eta}\vartheta^u_{mn}\right) - 1\right\}, \tag{D4}$$

where the Normal Probability Function P is (Abramowitz and Stegun 1968)

$$P(x) = \int_{-\infty}^{x} \frac{1}{\sqrt{2\pi}} e^{-t^2/2}\, dt. \tag{D5}$$

The integral of Eq.(D4) is evaluated over the vertical slice depicted in Fig. D2. By Eq.(D4) and $\vartheta^u_{mn} = \sqrt{p_0^2 - \bar{\phi}^2_{mn}}$,

$$\int_{\vartheta^l_{mn}}^{\vartheta^u_{mn}} \left|\mathcal{G}(\bar{\phi}_{mn},\bar{\theta})\right|^4 d\bar{\theta} = g_0^2\frac{\eta}{4}\sqrt{2\pi}e^{-8\bar{\phi}^2_{mn}/\eta^2}\left\{2P\left(\frac{4}{\eta}\sqrt{p_0^2 - \bar{\phi}^2_{mn}}\right) - 1\right\}.$$

To determine the accuracy of Eq.(D3), analyze the ratio

$$W(\bar{\phi}_{mn}) = \frac{\int_{-\infty}^{\infty}\left|\mathcal{G}(\bar{\phi}_{mn},\bar{\theta})\right|^4 d\bar{\theta} - \int_{\vartheta^l_{mn}}^{\vartheta^u_{mn}}\left|\mathcal{G}(\bar{\phi}_{mn},\bar{\theta})\right|^4 d\bar{\theta}}{\int_{-\infty}^{\infty}\left|\mathcal{G}(\bar{\phi}_{mn},\bar{\theta})\right|^4 d\bar{\theta}}$$

$$= 2\left\{1 - P\left(\frac{4}{\mu p_0}\sqrt{p_0^2 - \bar{\phi}^2_{mn}}\right)\right\}. \tag{D6}$$

As the ratio decreases, the accuracy of Eq.(D3) improves. Clearly, Eq.(D6) depends on how close $\bar{\phi}_{mn}$ is to p_0. In particular, by applying Table 26.1 of (Abramowitz and Stegun), W attains its maximum (minimum) value of unity (0.0144) when $\bar{\phi} = \pm p_0\,(0)$. The actual integral is 98.56% of the approximation for $\bar{\phi} = 0$, which is reasonably good; however, the approximation is the worst it can be at $\bar{\phi} = \pm p_0$.

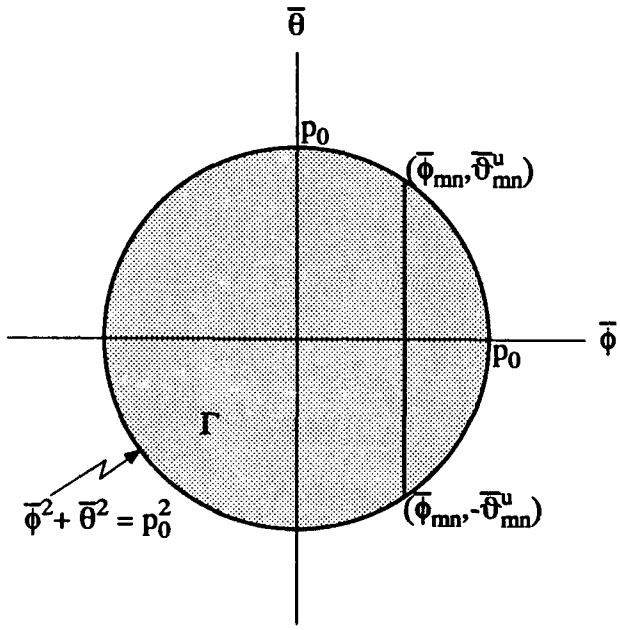

Fig. D2 – The region that is subtended by the Gaussian pattern's mainlobe in the coordinates $\bar{\phi}$ and $\bar{\theta}$

Let $\bar{\phi} = \lambda p_0$, $-1 \leq \lambda \leq 1$, correspond to an arbitrary $\bar{\phi}$–slice in the mainbeam (Fig. D2). Then the argument of P becomes $4\sqrt{1-\lambda^2}/\mu$. Since $W(\bar{\phi}) = 0.0930$ for $\lambda = 0.7273$, the approximation is still fair for all $|\bar{\phi}_{mn}| \leq 0.7273 p_0$. Although the approximation is not good for $|\bar{\phi}_{mn}| \in [0.7273 p_0, p_0]$, the amplitudes

$$g_0^2 \frac{\eta}{4} \sqrt{2\pi} \exp\left(-\frac{8\bar{\phi}_{mn}^2}{\eta^2}\right) \tag{D7}$$

of these contributions to the clutter-Doppler spectrum are < 0.20502 of the contribution at $\bar{\phi} = 0$ (see Fig. D3 and Table D1 for evaluations of $\exp(-8\bar{\phi}_{mn}^2/\eta^2)$). Consequently, they won't contribute as heavily to $S_{CL}(f)$. In particular, the spectral contributions for strips near the heel and toe of the mainbeam may be ignored. To determine whether the contributions in the transitional region, from $0.7273 p_0$ to a value a bit less than p_0, one must analyze them for each power gain on a case-by-case basis.

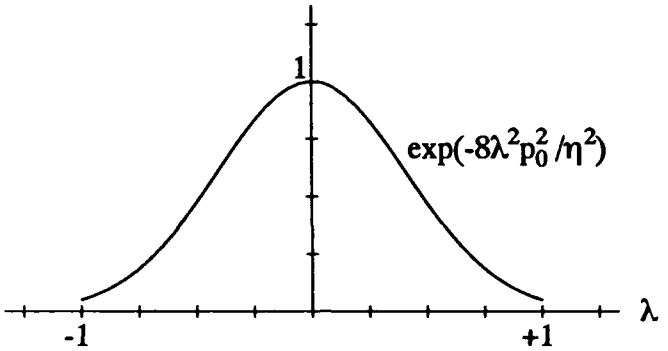

Fig. D3 — The exponential term of the amplitude in Eq.(D7) vs the fraction λ of the half-beamwidth p_0

Table D1 — Exponential vs λ

λ	$exp(-8\bar{\phi}^2/\eta^2)$
0.0000	1.00000
0.2500	0.82925
0.5000	0.47287
0.7273	0.20502
0.7500	0.18543
0.8000	0.14701
0.8500	0.11482
0.9000	0.08834
0.9500	0.06696
1.0000	0.05000

REFERENCE

M. Abramowitz and I. A. Stegun, ed., *Handbook of Mathematical Functions* (Dover Publications, Inc., New York, 1968), p. 970.